**IEEE Transactions on Robotics (T-RO) paper, presented at ICRA 2026, Vienna, Austria. Cite as T-RO paper.**

# CCRobot-S: A Robotic Cable-Climbing Squad Collaborating for Fast Inspection and Heavy-Duty Maintenance

Zhenliang Zheng[1,2,†], Ning Ding[2,†,*], Herbert Werner[3], Feng Ren[2],
Yongyuan Xu[1,3], Wenchao Zhang[2], Xiaoli Hu[2], Jianguo Zhang[2], and Tin Lun Lam[1,2,*]

***Abstract*—This study introduces a novel climbing strategy, reconfigurable parallel-type cable-driven climbing designed for long-span, large-scale bridge stay cable robotic applications, which has the potential to revolutionize the stay cable inspection and maintenance practice. The proposed methodology features the development of a Collaborative Climbing Robot Squad (CCRobot-S), which builds upon the design principles of the previous CCRobot series. In this study, CCRobot-S implements a parallel-type cable-driven manipulation design, allowing for reconfigurable kinematic morphology by its movable anchor bases and realizing the capacity of crossing over the stay cables for its flying platform. The collaborative robot squad design liberates the dimensions and scales of the robot's reachable workspace and moves the part of the robotic system that indeed needs to be moved, enhancing the working efficiency and climbing agility. This strategy also utilizes controllable adhesion instead of friction to interact with the bridge cable surface for the flying platform, realizing force multiplication for forceful manipulation. Toward bringing high efficiency and heavy-duty capacity, we propose the applicable climbing frameworks (zero-downtime climbing gait for cable inspection and spider-like climbing gait for cable maintenance) and the optimization frameworks (optimal anchor configuration for the movable anchor bases and optimal grasp arrangement for the flying gripper). This article includes the exploration of the design and climbing gaits of CCRobot-S, the formulation of the CCRobot-S model, a comprehensive analysis of its workspace, and its climbing strategy and optimization. Extensive experiments have assessed the proposed climbing strategy's effectiveness and showcased CCRobot-S' capabilities.**

***Index Terms*—CCRobot Squad, climbing robot, cable inspection and maintenance, movable anchor base, reconfigurable parallel-type cable-driven climbing.**

## I. INTRODUCTION

LONG-SPAN, large-scale cable-stayed bridges, exemplified by the Hong Kong-Zhuhai-Macau Bridge, are frequently constructed in challenging and exposed environments, spanning ravines, mountains, valleys, lakes, rivers, seas, and urban structures. However, the bridge cables, the primary components of cable-stayed bridges, are highly susceptible to various forms of deterioration due to temperature fluctuations, mechanical loading, corrosion of strand bundles, and so on, leading to potential safety hazards. Regular inspections are crucial for identifying cable defects and deterioration points, ensuring the stay cables' structural integrity and safety. Surveys conducted in Europe and North America have revealed significant degradation in many existing bridge cables, highlighting the necessity for prompt repair and maintenance interventions [1].

### *A. State of the Art*

Various cable-climbing robots have been developed to inspect and maintain bridge cables. The majority of these robots, as documented in the literature, are focused on stay cable inspection [2]–[8], with only a limited number dedicated to cable maintenance tasks such as stay cable cleaning, repair, coating, and grinding [9]–[12]. One notable example is the MRCIN-II cable-climbing robot designed for cable inspection by Kyeong Ho Cho et al. [2], [4]. This robot features caterpillar tracks instead of wheels, enabling smooth movement on the uneven surface of the stay cable. Fengyu Xu et al. [9] have proposed a cable maintenance robot based on a quadrilateral independent suspension system. The robot is equipped with simple grinding, cleaning, spray-coating, and winding mechanisms to address surface damage points automatically. Additionally, our team has developed the CCRobot series [13]–[20], comprising five generations of cable-climbing robots aimed at enhancing climbing speed and load capacity simultaneously in an autonomous climbing system.

As can be observed from Tab. I, despite some available cable-climbing systems that have been tested in laboratory and field environments, and some bridge climbing robots have been applied and deployed in the field [25]–[30], challenges still remain to improve the performance of the cable inspection and maintenance robotic systems.

**Efficiency and Agility:** With the continuous technological advancements in civil infrastructure, the prevalence of super-long-span cable-stayed bridges has increased worldwide. Consequently, the operational scope and scale that robotic systems need to accommodate have expanded significantly, from the

---

This work was partly supported by Shenzhen Science and Technology Program (grants GJHZ20240218114202004, 20220817171811004), Guangdong Provincial Leading Talent Program (grant 2024TX08Z319), National Natural Science Foundation of China (grant 62106155), Guangdong Basic and Applied Basic Research Foundation (grants 2023A1515012570, 2021B1515420005), Shenzhen Major Science Technology Project (grant KJZD20230923114810022), and the Longgang District Shenzhen's "Ten Action Plan" for Supporting Innovation Projects (grant LGKCSDPT2024002).

(†*These authors contributed equally to this paper.*) (**Corresponding authors: Ning Ding, Tin Lun Lam. Email:* {`dingning, tllam`}`@cuhk.edu.cn`)

[1] School of Science and Engineering, The Chinese University of Hong Kong (CUHK), Shenzhen, 518172, China.

[2] Shenzhen Institute of Artificial Intelligence and Robotics for Society (AIRS), Shenzhen, 518172, China.

[3] Institute of Control Systems, Hamburg University of Technology (TUHH), Hamburg, 21073, Germany.

**IEEE Transactions on Robotics (T-RO) paper, presented at ICRA 2026, Vienna, Austria. Cite as T-RO paper.**

TABLE I
PERFORMANCE COMPARISON

| Robots | Robot Type | Functional Implementation | Weight (kg) | Payload (kg) | Speed (m/min) | Reconfiguration Mechanisms | Cable-Crossing Capacity |
|---|---|---|---|---|---|---|---|
| CMR 1 [10] | Individual Robot | Painting | 160 | 140 | N/A | × | × |
| PCMR [11] | Individual Robot | Cleaning; Painting | 75 | N/A | N/A | × | × |
| CMR 2 [12] | Individual Robot | Cleaning; Spraying | 80 | 150 | 2∼8 | × | × |
| 3DClimber [8] | Individual Robot | Inspection | 42 | 1 | N/A | × | × |
| MRC$^2$IN-I [2] | Individual Robot | Inspection | 30 | 9 | 2.1 | × | × |
| MRC$^2$IN-II [4] | Individual Robot | Inspection | 30 | N/A | 3.6 | × | × |
| Bilateral Robot 1 [21] | Individual Robot | Inspection | 5 | 4 | $\leq$ 13.5 | × | × |
| Bilateral Robot 2 [22] | Individual Robot | Inspection | 4 | 1.5 | $\leq$ 9.9 | × | × |
| Trilateral Robot [23] | Individual Robot | Inspection | N/A | 3.2 | $\leq$ 13.5 | × | × |
| Treebot [24] | Individual Robot | Inspection | 0.6 | 1.75 | 0.733 | × | × |
| CCRobot-I [14] | Individual Robot | Internal Inspection | 15 | 30 | 3 | × | × |
| CCRobot-II [15] | Individual Robot | Internal Inspection | 25 | 30 | 5.2 | × | × |
| CCRobot-III [16] | Multi-Robots | Internal Inspection | 28.3 | 40 | 12 | ✓ | × |
| CCRobot-S | Multi-Robots | Grinding; Repair | 36 | 30 | 15 | ✓ | ✓ |

meter level to hundreds or even thousands of meters. For example, the Russky Bridge [31] in Vladivostok, Primorsky Krai, Russia, stands as one of the longest cable-stayed bridges, spanning a total length of 3100 meters, with towers reaching a height of 324 meters. Featuring 168 super-long cables, the longest stay cable measures 579.83 meters. Rough estimations indicate that the inspection and maintenance area, enclosed by the perimetrical cables, spans approximately one million square meters. Notably, existing climbing robotic systems do not align in dimensional scale and workspace with structures of such magnitude, rendering conventional systems inefficient for inspection and maintenance tasks. Despite enhancing accessibility, previous robotic systems entail intricate and time-consuming preparatory and installation procedures. Clamp mechanisms, commonly employed on cable-climbing robots for friction-based locomotion (wheel/caterpillar) or adhesion (gripper/palm) on stay cables, pose challenges during installation. In some cases, specialized adhesion tools are devised for robot installation [4]. Moreover, when the self-weight of an individual cable-climbing robot is excessive, the use of auxiliary equipment such as cranes, bucket trucks, or hydraulic lifts becomes essential for its operation [32]. Operators must repeatedly install and uninstall the robot on each stay cable, a process that typically takes 30 to 60 minutes per cable. Given that long-span cable-stayed bridges often have hundreds of stay cables, these repetitive installation and removal procedures consume a significant portion of the overall inspection and maintenance time. Consequently, achieving efficient and agile inspection and maintenance of these large-scale multi-cable bridge components poses a significant challenge in robotic inspection and maintenance science.

**Load Capacity and Forceful Manipulation:** Literature reveals a classification of cable-climbing robots into two distinct groups based on their intended design purpose and functionality: cable inspection robots and cable maintenance robots. Most research in this domain focuses on carrying detection sensors for cable inspection tasks, such as cable surface vision inspection, rather than concentrating on cable maintenance. Inspection activities typically require robots to carry low loads. However, maintenance tasks necessitate the inclusion of one or dual six/seven Degree of Freedom (DoF) robotic manipulators and specialized maintenance tools or end effectors, such as grinding heads, milling heads, hot melt guns, coating guns, cleaning heads, and winding devices. Typically, the total weight of a six/seven DoF robotic manipulator and a specialized tool or end effector exceeds 20 kg. Conventional wheel-based climbing robots, whose weight is normally more than 40 kg, often struggle to accommodate such heavy combinations directly due to their limited load capacity. Our research delves into the detailed reasons behind the low load capacity of wheel-based climbing robots [14]–[16]. Furthermore, cable maintenance operations introduce dynamic loads and impacts from contact forces during grinding, milling, or repair processes, necessitating cable maintenance robots to withstand and overcome these effects. Therefore, the load capacity of climbing maintenance robots is constrained. Additionally, the protective layers of bridge cables limit the robot's load capacity. Unlike wire ropes without protective layers, stay cables are typically protected by high-density polyethylene (HDPE). This material is relatively soft and more susceptible to damage under high-load conditions. The shear forces and increased extrusion pressures resulting from high loads can cause significant wear and tear on the HDPE protective layer. Consequently, achieving a high payload capacity for cable-climbing robots remains a significant challenge, particularly for cable maintenance on relatively soft cable protective layer materials.

**Versatility and Agility:** Versatility and agility have been the prerogative of small-scale, terrestrial robots in gravity-cooperative environments, as per the scaling law. Examples include Boston Dynamics' Spot [33], Zurich's StarlETH [34], and MIT's cheetah [35], which are developing toward closing the performance gap between robots and their biological counterparts. However, for cable-climbing robots, the criteria for achieving versatility and agility differ significantly. As we have analyzed, the sizes of infrastructure components continue to increase, and small-sized robots face limitations in mobility and efficiency for inspection and maintenance tasks. A heavy, large-scale cable-climbing robot may be favored for its ability to carry more powerful specialized tools or end effectors and to support greater computational resources. However, this comes at the cost of reduced versatility and agility compared to

**IEEE Transactions on Robotics (T-RO) paper, presented at ICRA 2026, Vienna, Austria. Cite as T-RO paper.**

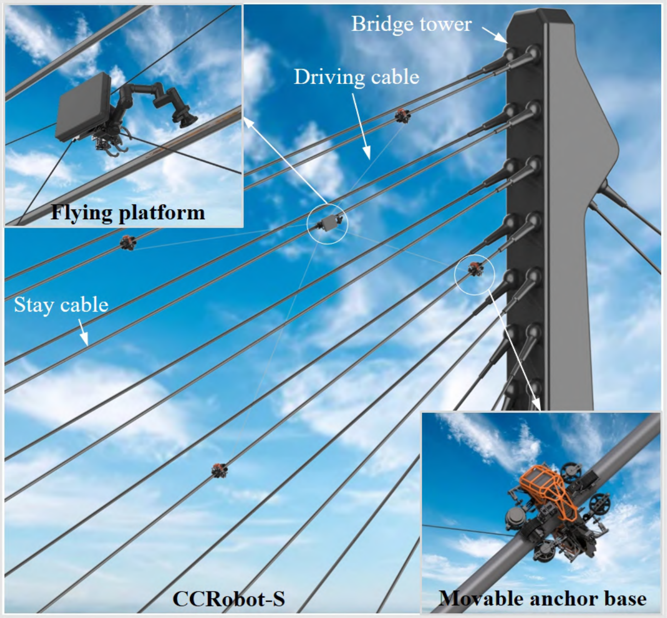

Fig. 1. CCRobot-S: a collaborative climbing robot squad developed for high efficiency, heavy payload, and versatility & agility.

smaller models. Moreover, when a cable-climbing robot navigates on stay cable surfaces in gravity-defying scenarios, its climbing performance and maneuverability are often restricted to rudimentary tasks, limited load capacities, or low climbing speeds. Consequently, the attainment of versatile and agile characteristics in an anti-gravity large-scale environment poses a formidable challenge for a cable-climbing robotic system.

### B. Contribution

Analyzing the state-of-the-art cable-climbing robots for inspection and maintenance reveals that the existing solutions can not unite high efficiency, heavy payload, and versatility & agility into one system. Most robots possess only one of these core characteristics, neglecting their performance on the others. Toward combining these advantages of efficiency, payload, and versatility & agility, we developed a **C**ooperative **C**limbing **R**obot **S**quad (**CCRobot-S**) for stay cable inspection and maintenance, as shown in Fig. 1. This system is composed of a moving platform – Flying Platform – which could integrate a robotic manipulator or specialized inspection and maintenance tools, and four wheel-based cable-climbing robots – Movable Anchor Bases – which are similar to our previous climbing precursor of CCRobot-V [19]. Each movable anchor base is equipped with a customized winch, and it is connected with a fixed cable attachment point on the flying platform, which is driven and manipulated by the four parallel cables together. Meanwhile, the flying platform can adhere to the bridge cable with its flying gripper. Then, the movable anchor bases would move on the stay cable to a designated position and attach themselves to the cable, thereby reconfiguring the geometry enclosed by the four movable anchor bases.

The contribution of this paper is manifold and can be summarized as follows:

- CCRobot-S adopts a novel collaborative climbing robot squad, combining high efficiency, heavy-duty capacity, and versatility & agility, advancing state-of-the-art climbing technology. It holds promise for practical applications in the stay cable inspection and maintenance. Furthermore, the proposed methodology for reconfigurable parallel-type cable-driven climbing establishes an innovative climbing paradigm for scenarios with challenging gravity-adversarial large-scale conditions, opening the opportunity and paving the way for developing high-quality climbing robotics. Researchers can leverage this approach as a foundation for designing climbing systems in diverse applications.
- In contrast to a conventional individual cable-climbing robot, the reconfigurable morphology and collaborative design of CCRobot-S liberate the dimensions and scales of the reachable workspace, implementing by coiling or uncoiling the driving cable wound around the customized winch and by adjusting the attachment points via the movable anchor base. Meanwhile, the cable length can be sufficiently long relative to the size of the robotic structure, affording CCRobot-S the possibility of workspace expansion. CCRobot-S distributes the system's total weight into several lightweight agents to move the part that indeed needs to be moved. The robot that needs to be installed on the stay cable is the movable anchor base, which weighs only 9 kg. It can be easily installed on the stay cable by only one person. Furthermore, CCRobot-S realizes the capacity of crossing over the stay cables for the flying platform, eliminating the repetitive installation procedures. As a result, efficiency promotion and climbing agility are achieved.
- CCRobot-S exploits controllable adhesion instead of friction to interact with the bridge cable surface through the gripper and winch [16]–[18]. Four customized winches mounted on the movable anchor bases are adopted to pull the flying platform. By distributing the load across multiple movable anchor bases, the lift force is generated by the combined action of multiple forces resulting from the pulling of the multiple winches, rather than by the frictional force produced by the extrusion between the wheels and the cable surfaces. As such, the gravity-defying locomotion of the flying platform is decoupled from the friction on the bridge cable surfaces. In that case, the robot squad can pull a substantial load compared to its weight, which makes it highly suitable for more versatile tasks. Thereby, the robot team achieves a collaborative effect, and force multiplication for forceful manipulation is realized.
- CCRobot-S proposes a novel task-based climbing strategy, including the zero-downtime climbing gait for stay cable inspection and the spider-like climbing gait for stay cable maintenance. An optimal anchor configuration for the kinematic morphology of CCRobot-S is developed to improve the stability and accessibility of the inspection devices with a given trajectory under the wrench-closure conditions. In addition, an optimal grasp arrangement algorithm for the flying gripper is proposed to ensure

**IEEE Transactions on Robotics (T-RO) paper, presented at ICRA 2026, Vienna, Austria. Cite as T-RO paper.**

that the gripper can attach to the desired position from the perspective of robustness and manipulability under wrench-closure conditions and grasping region range constraints for cable maintenance.

### C. Structure of the Paper

The structure of the remaining sections in this paper is outlined as follows. Section II will first address the design principles and underlying philosophy of CCRobot-S, followed by an in-depth exploration of the mechanical design and climbing gaits of CCRobot-S. Before determining the climbing strategy of CCRobot-S, the model of CCRobot-S is analyzed and formulated in Section III, and the admissible workspace on the climbing region is identified and analyzed comprehensively in Section IV. Then, we conduct the climbing strategy and the optimal control in Section V. Section VI presents the prototype and experiments. Finally, conclusions and future works are drawn in Section VII.

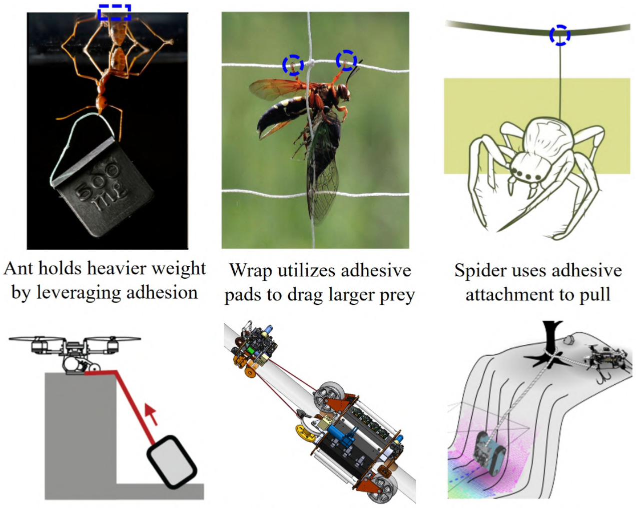
Ant holds heavier weight by leveraging adhesion
Wrap utilizes adhesive pads to drag larger prey
Spider uses adhesive attachment to pull
FlyCroTug，Stanford
CCRobot-III，CUHKSZ
UAV/UGV，UTokyo

Fig. 2. Winch gait found in nature (up) [37], [42], [43], and bio-inspired climbing robots that adopt this principle and strategy (down) [16], [37], [44].

## II. DESIGN OF CCROBOT-S

### A. Design Philosophy

To develop a comprehensive robotic platform for stay cable inspection and maintenance without compromising performance, we explore the climbing gaits broadly. Three climbing gaits are defined based on the robot's contact state with the climbing substrates: Smooth Gait, Impulsive Gait, and Winch Gait, as illustrated in Tab. II. The smooth gait means the robot can provide a consistent contact force with the climbing object surface. Most wheel/track-based climbing systems [2]–[7] and a part of leg/palm-based climbing systems [8], [38]–[40] adopt this gait to climb, primarily for rapid climbing speed. However, these systems have substantial payload limitations because the contact area between their wheels and the climbing objects is a point or line. Alternatively, impulsive gait has an airborne phase. Some terrestrial running robots like Mini Cheetah [41] are impulsive. However, due to the sophisticated dynamic balance condition and gravity-defying property, impulsive gait is rarely used on climbing robots. RiSE2 [36] is one of these kinds of robots. Winch gait, inspired by nature [37], [42], [43], as shown in Fig. 2, takes advantage of the pull or tug force intelligently. The locomotion strategy is for the robot to adhere to a substrate to exploit controllable adhesion. Then, it pulls the payload, whose weight always exceeds the robot's, by a winch or similar mechanism. The stroke step length can be long enough compared to the robot's own body length. This phenomenon and strategy are also found in nature. For instance, a spider can anchor itself on the sticky threads and then haul and manipulate its prey by another type of thread – smooth threads [43].

In recent years, some researchers have adopted this bio-inspired principle to design climbing robotics [37], [44]–[46]. For instance, Stanford University developed the FlyCroTugs [37], which could adhere the Micro Air Vehicles (MAVs) to a surface and tug up to 40 times their mass. R. R. Sudiono et al. from Tokyo Institute of Technology [46] developed a mobile cable anchor with a winding machine. Two mobile cable anchors can pull an end-effector together by their winding machines. Our team has also previously developed a series of tree-climbing robots (Treebot series) [24], [47]–[49] and cable-climbing robots (CCRobot series) [16]–[19] based on this idea and principle.

Although these robotic prototypes have successfully achieved some desired capacities, several issues remain with this robotic solution. First, the winch-gait mode of locomotion typically means that two robots are connected with a flexible medium, allowing one robot to anchor on a certain type of substrate and pull another. While in this process of pulling, the whole system is under-actuated, and the locomotion of the object being pulled is always accompanied by oscillation, which is not desirable for inspection and maintenance. Furthermore, the connecting medium of the winch-gait robots is always only a cable. Once the cable is broken, the object being pulled may fall from a high place, causing serious damage to the robot and potential security risks. Meanwhile, most of the existing winch-gait robots only explore forward locomotion. However, backward locomotion is rarely considered. Therefore, how to return to the initial location is still an issue for the winch-gait climbing robots. Imagine a winch-gait climbing robot is applied in a vertical environment: when the object being pulled climbs down, it is driven by gravity, and the process is uncontrollable, which is an underlying risk for the entire climbing process. In addition, the workspace of the winch-gait climbing robot is barely satisfactory. For instance, CCRobot-III [16] and CCRobot-IV [17] are constrained to a stay cable, and they can not cross over the stay cables, which leads to low working efficiency.

To further optimize the winch gait and improve the performance of CCRobot-III [16] and CCRobot-IV [17], an innovative climbing system – CCRobot-S – is developed. As a spider creates a sizeable tensile structure between fixed attachments [43], CCRobot-S configures a parallel-type cable-driven manipulation. At the same time, the counterparts of the fixed attachments of the tensile structure are movable in the CCRobot-S system. Every agent in the system can fasten itself onto the stay cable. The main idea and design principle

TABLE II
DESIGN PHILOSOPHY

| Climbing Gait | Typical Robots | Inspiration | Design Principle | Specific Capabilities | Limitations |
|---|---|---|---|---|---|
| Smooth Gait | MRC$^2$IN-I,II [2], [4] | N/A | Wheel/track-based climbing | Rapid speed | Payload capacity |
| Impulsive Gait | RiSE2 [36] | Cheetah | Leg/palm-based climbing | Airborne phase | Sophisticated balance |
| Winch Gait | FlyCroTugs [37] | Ant; wrap; spider | Controllable adhesion instead of friction | Heavy payload | Underactuated system |
| Spider Gait | CCRobot-S | Spider and spider web | Reconfigurable morphology; collaborative climbing | Force multiplication; workspace expansion; versatility and agility | / |

of CCRobot-S is harnessing controllable adhesion rather than friction to interact with the climbing substrates to augment the load capacity for forceful manipulation. The reconfigurable morphology and collaborative design of CCRobot-S break through the robot's structural size limitations. This innovation expands the reachable workspace and distributes the system's weight into several lightweight agents. By moving the part that indeed needs to be moved, the design improves working efficiency and climbing agility. Additionally, actuation redundancy realized by four driving cables is beneficial to the attainment of intrinsic safety for the robotic system. Even if the phenomenon of a driven cable failure occurs, the platform's position can be constrained by the remaining driving cables rather than the platform rushing or crashing to an undesired position, causing dangerous and devastating situations.

### *B. Mechanical Design*

As illustrated in Fig. 1, CCRobot-S comprises four cable-climbing robots serving as the movable anchor bases on the stay cables, along with a flying platform capable of accommodating a robotic manipulator, end effectors, specialized tools, or sensors for stay cable inspection and maintenance. Each movable anchor base is connected to the flying platform through a DYNEEMA@ cable.

**Flying platform** is the crucial component of the robot team in CCRobot-S. Unlike the conventional Unmanned Aerial Vehicle (UAV), the flying platform can traverse and hover in a defined geometric space delineated by the four movable anchor base points. Furthermore, it can perch on and cling to the stay cable while approaching it. Overall, it functions as a multi-modal aerial vehicle. Fig. 3 shows the proposed Computer-Aided Design (CAD) model of the flying platform. It comprises several key components: an adhesion mechanism known as the flying gripper, a three Degree-of-Freedom (DoF) joint for adjusting the pose of the flying gripper, a robotic manipulator, a specialized tools unit, and a control cabinet. Four fixed cable attachment points are uniformly distributed around the holder of the control cabinet, forming a square. The total weight of the platform is approximately 30 kg.

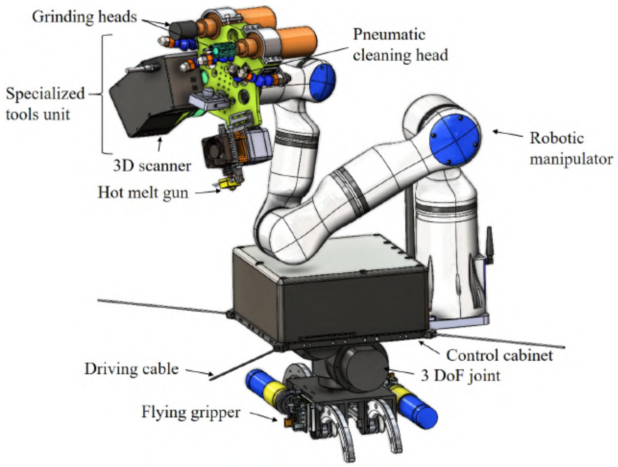

Fig. 3. Structure of the flying platform, which integrates with a robotic manipulator and a specialized tools unit.

1) The 3 DoF joint can adjust the position and attitude of the flying gripper to approach and grasp the stay cable. Three serial EC servo motors drive it, and every motor integrates a planetary gear with a reduction ratio of 36:1 and a brake to bear the gravity of the flying platform when it adheres to the stay cable.

2) The flying gripper is mounted at the end of the 3 DoF joint. The design for the gripping module of CCRobot-S follows the style of the CCRobot series [14]–[16] that we have developed. The kinematic transmission and the appearance are consistent, aiming at maximizing power delivery and maintaining energy conservation.

3) A seven Degree-of-Freedom (DoF) robotic manipulator has been chosen for cable maintenance tasks due to its flexibility and reachability, particularly towards the rear section of the stay cable.

4) The specialized tools unit consists of a grinding head, a hot melt gun, a pneumatic cleaning gun, a vision sensor, and a laser 3D scanner.

**Movable anchor base** is a wheel-based cable-climbing robot (see Fig. 1). The structure of the movable anchor base is analogous to the precursor of CCRobot-V [19], both equipped with a locomotion mechanism (driving wheel unit) and an adhesion mechanism (gripper unit). Besides, a customized winch is incorporated into the movable anchor base, with one of the driving cable attachment points fixed on the winch. To simplify the installation process, we further optimized the structure and size with a compact and lightweight design, resulting in each movable anchor base weighing approximately 9 kg. In the CCRobot-S system, the movable anchor base functions as a movable cable attachment point. By relocating the four movable anchor points, the kinematic morphology of CCRobot-S can be reconfigured.

### *C. Gait Design and Analysis*

Before introducing the gait design and analysis, the electrical architecture of the CCRobot-S system that implements the climbing gait is presented as shown in Fig. 4, which outlines the electrical components and their connections within the CCRobot-S system. The architecture consists of two

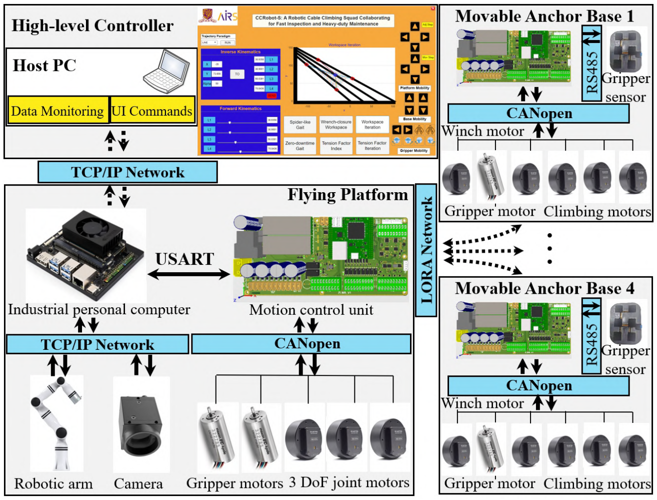

Fig. 4. The electrical architecture of the CCRobot-S system: the electrical components and their connections within the robotic system.

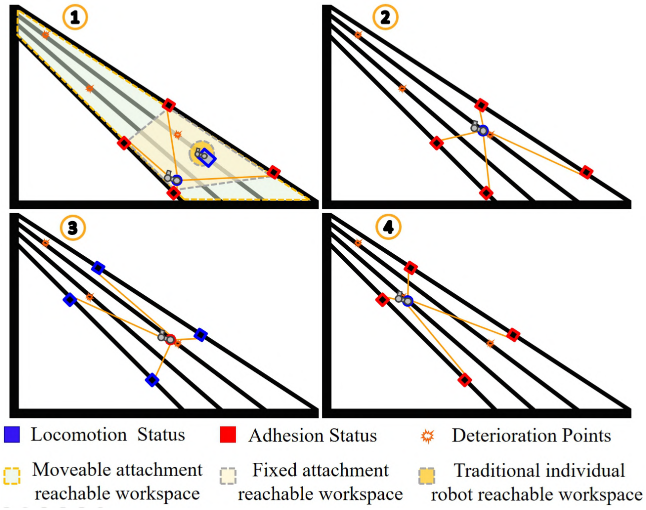

Fig. 5. Schematic diagram of the spider-like climbing gait for stay cable maintenance, and the comparison of admissible workspace between CCRobot-S and a similarly sized individual robot.

subsystems: a remote controller and an onboard controller that communicate with each other by Transmission Control Protocol/Internet Protocol (TCP/IP). The onboard controller is responsible for controlling five sub-robots: one flying platform and four movable anchor bases. The communication between the flying platform and the movable anchor bases is supported by a Long Range Wide Area Network (LoRaWAN), which facilitates robust one-to-many communication from a central host to multiple slaves simultaneously.

In the CCRobot-S system, the locations of the movable anchor bases predominantly dictate the system's movement, i.e., the positions of the four movable anchor bases can significantly influence the motion of the flying platform. Meanwhile, whether the flying platform perches on the stay cable can affect the design of the climbing gait. In this paper, we distinguish between two fundamentally alternative approaches for motion generation, which are decided by the climbing objective/task: spider-like climbing gait for stay cable maintenance requiring the transportation of heavy load devices such as robotic manipulators or specialized tools; zero-downtime climbing gait for stay cable inspection which only needs to carry a high-definition camera.

*Spider-like Climbing Gait*: As discussed in Section II-A, the spider-like climbing gait is the evolving version of the winch gait. We highlight this gait since it can produce a heavy-load capacity for stay cable climbing, harnessing controllable adhesion instead of friction to interact with the stay cables and augment the load capacity for forceful manipulation. Fig. 5 shows the schematic diagram of the gait decomposition when CCRobot-S is climbing up on the stay cables. It illuminates that the flying platform is driven by the four cables attached to the movable anchor bases in Phase 1. When the flying platform approaches the deterioration point, it shifts from the locomotion status to the adhesive status by utilizing its flying gripper to fasten onto the stay cable and then to repair the deterioration point through the specialized tools in Phase 2. After the maintenance work, the four movable anchor bases loosen their grippers and move along the stay cable to relocate their positions in Phase 3. In Phase 4, the flying platform detaches from the stay cable and moves to another deterioration point. At this point, a climbing cycle of CCRobot-S for a spider-like climbing gait is completed.

*Zero-downtime Climbing Gait*: Zero-downtime climbing gait is used to rapidly inspect the stay cable to detect the potential deterioration point that needs to be maintained. This gait leverages the flying platform's cable-crossing ability to traverse and approach multiple stay cables' surfaces in sequence within the area enclosed by the four movable anchor base points without the robots' repetitive installation and de-installation processes. Fig. 6 shows the schematic diagram of the gait decomposition when CCRobot-S is climbing up on the stay cables. It demonstrates that the flying platform continuously moves along several stay cables from Phase 1 to Phase 2. After completing the rough inspection in the initial region enclosed by the four movable anchor base points, the movable anchor bases would detach themselves from the stay cables and move to other positions to commence the next phase of the task. It is worth mentioning that during the whole climbing process, the flying platform does not need to perch on and cling to the stay cable since it only consists of lightweight inspection tools. The four movable anchor bases can carry it together through the tension of the driving cables during movement.

With the analysis of climbing gaits, it is evident that CCRobot-S provides an outsized reachable workspace by a comparatively small robot squad through deployable multiple agents – movable anchor bases and reconfigurable architecture. i.e., a small robot team for large-scale mobile manipulation is realized. Due to the winch mechanisms, CCRobot-S' mass, size, and complexity do not scale with its rising capacity of accessibility and reachability. In contrast, a traditional rigid-link individual robot designed for comparable tasks must withstand substantial bending forces, high energy consumption, and more powerful actuators. As depicted in Figs. 5 and 6, the admissible workspace of CCRobot-S significantly exceeds that of a comparably sized individual robot. This advantage holds true regardless of whether the attachments are fixed

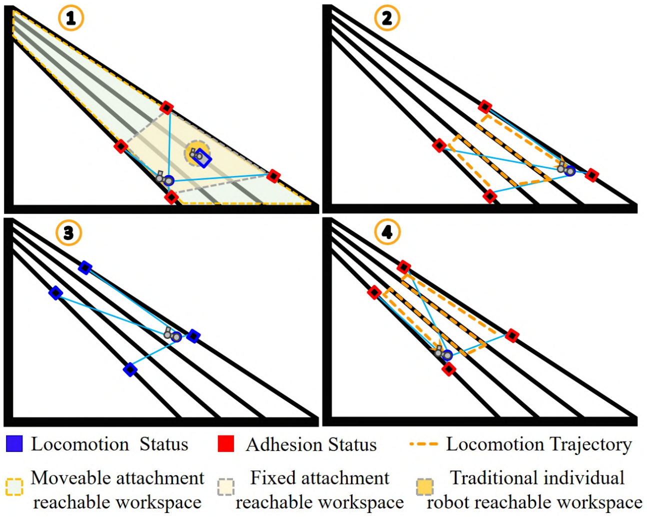

Fig. 6. Schematic diagram of the zero-downtime climbing gait for stay cable inspection, and the comparison of admissible workspace between CCRobot-S and a similarly sized individual robot.

or movable. Although only two target cables are depicted in the schematic diagram, the system can cover more cables by adjusting the positions of the movable anchor bases to different stay cables. This flexibility is crucial for large-scale bridge inspection and maintenance tasks with numerous stay cables. Moreover, the climbing gait employed by CCRobot-S allows the flying platform to easily fly over obstacles on the stay cables, which would pose challenges for the conventional individual robot. What is worth noting is that the workspace discussed here is estimated roughly rather than calculated with a numerical or analytical approach precisely under the wrench-closure condition, which is further presented in Section IV.

## III. MODEL OF CCROBOT-S

Based on the climbing gait analysis for CCRobot-S, we break down CCRobot-S' motion into three modes: the "body movement" stage, where all four movable anchor bases remain anchored to the surfaces of stay cable while the flying platform maneuvers within the enclosed region defined by the four movable anchor base points; the "tail end movement" stage, where the flying platform fastens itself onto the stay cables while the four movable anchor bases move to desired new anchor points; and the "whole squad movement" stage, where the flying platform and the movable anchor bases move cooperatively in space. By alternating between the "body movement" stage of motion and the "tail end movement" stage of motion, the spider-like climbing gait is generated, or by alternating between the "body movement" stage of motion and the "whole squad movement" stage of motion, the zero-downtime climbing gait is generated.

For the "tail end movement" stage of motion, its model is similar to the traditional wheel-based cable-climbing robots, which have been established and analyzed in our previous cable-climbing robot: CCRobot-V [19] as well as some other conventional cable-climbing robots, thereby, in this work, we focus on the model of the "body movement" stage of motion and the more general model of the "whole squad movement" stage of motion and make the following assumptions: First, we omit the rotation disturbances around the stay cable of the movable anchor bases; Second, the flying platform and movable anchor bases are treated as rigid bodies with point masses; Third, the driving cables' mass is assumed to be negligible compared to that of the flying platform and movable anchor bases, and their elasticity and sagging are neglected; Also, considering that the kinematic and dynamic interactions of CCRobot-S primarily occur within the plane defined by the four movable anchor base points, a 2D planar adaptation is utilized to formulate the model of CCRobot-S.

**Kinematics** Fig. 7 shows the general model and the configuration of CCRobot-S. In the notation, the superscripts $l$ and $g$ denote the local frame of the flying platform and the global frame, respectively, and the script $M$ and $m$ denote the mass of the flying platform and the movable anchor base, respectively. The 3-DoF system (whose pose comprises translation and rotation) of the flying platform, driven by four cables, has the generalized coordinates, expressed as vectors: $\mathbf{x} = [\mathbf{p}^{\mathbf{T}}\mathbf{r}^{\mathbf{T}}]^{\mathbf{T}} \in \mathbb{R}^3$, where $\mathbf{p} \in \mathbb{R}^2$ and $\mathbf{r} \in SO_1$ denote the position and orientation of the flying platform, respectively. The velocity and acceleration of the flying platform are denoted by $\dot{\mathbf{x}}$ and $\ddot{\mathbf{x}}$, respectively. ${}^g\mathbf{A}_i = [A_{ix} \quad A_{iy}]^{\mathbf{T}}$ ($i$ = 1, 2, 3, 4) represents the movable anchor base's Cartesian translation relative to the global coordinate frame $\{\mathbf{g}\}$, and its orientation is correlative with the inclination angle of the stay cable $\boldsymbol{\alpha}$ or $\boldsymbol{\beta}$. ${}^l\mathbf{B}_i = [B_{ix} \quad B_{iy}]^{\mathbf{T}}$($i$ = 1, 2, 3, 4) represents the cable attachment location of the flying platform relative to the local coordinate frame $\{\mathbf{l}\}$. In this work, since the anchor base is movable and constrained along the stay cable, which is a one-dimensional reconfiguration, the reconfigurable points ${}^g\mathbf{A}_i$ can be modeled as ${}^g\mathbf{A}_i = [A_{ix}(u_i) \quad -tan(\alpha \vee \beta)A_{ix}(u_i) + tan(\alpha \vee \beta)(s_1 \vee s_2)]^{\mathbf{T}}$ ($i$ = 1, 2, 3, 4) with variable $u_i$. Consequently, the reconfiguration path of the movable anchor base can be described by a polynomial function of $u_i$, where $\boldsymbol{\alpha}$, $\boldsymbol{\beta}$, $s_1$, and $s_2$ are constants and their values can be measured for any cable-stayed bridge. Applying a vector loop on the model of CCRobot-S, as shown in Fig. 7, the closure constraint can be expressed as

$$\mathbf{BA}_i(u_i) + {}^g_l\mathbf{R}(\mathbf{r})^l\mathbf{B}_i + \mathbf{p} - {}^g\mathbf{A}_i(u_i) = 0; \quad i = 1,2,3,4, \tag{1}$$

where ${}^g_l\mathbf{R}(\mathbf{r})$ is the rotation matrix between coordinate frames $\{\mathbf{g}\}$ and $\{\mathbf{l}\}$.

For the "body movement" stage of motion of CCRobot-S, the system is similar to a cable-driven parallel manipulator, which is fully constrained since it possesses $n = 3$ degrees of freedom and $m = 4$ driving cables, where $n = m - 1$ [50]. The variables $u_i$ are constant, and the position of the movable anchor base is fixed. The segment $\mathbf{BA}_i$ of the cable $i$ can be rewritten as

$$\mathbf{BA}_i = {}^g\mathbf{A}_i - {}^g_l\mathbf{R}(\mathbf{r})^l\mathbf{B}_i - \mathbf{p}; \quad i = 1,2,3,4. \tag{2}$$

For the "whole squad movement" stage of motion of CCRobot-S, the position of the movable anchor base is changeable, and the system is kinematically redundant with the introduction of the linear joints of the movable anchor bases, the segment $\mathbf{BA}_i$ of the cable $i$ can be expressed as

$$\mathbf{BA}_i(u_i) = {}^g\mathbf{A}_i(u_i) - {}^g_l\mathbf{R}(\mathbf{r})^l\mathbf{B}_i - \mathbf{p}; \quad i = 1,2,3,4. \tag{3}$$

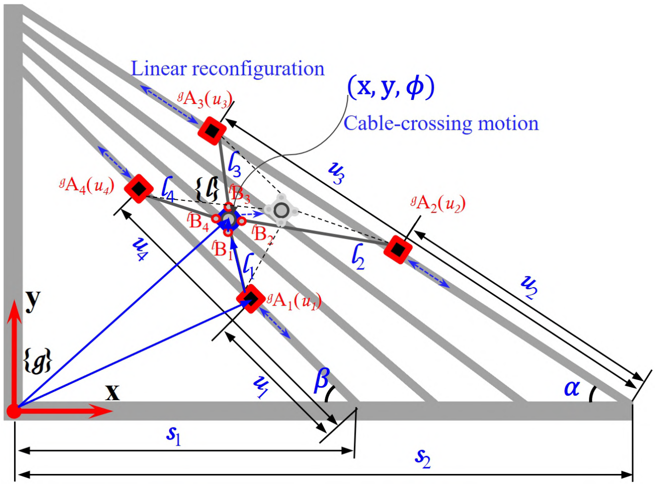

Fig. 7. The general model and configuration of CCRobot-S, which illustrates the flying platform and the movable anchor bases with their respective coordinate frames.

Furthermore, this can be rewritten as polynomial functions with variable $u_i$ as

$$\mathbf{BA}_i(u_i) = \begin{bmatrix} A_{ix}(u_i) - x \\ A_{iy}(u_i) - y \end{bmatrix} - \begin{bmatrix} \cos\phi & -\sin\phi \\ \sin\phi & \cos\phi \end{bmatrix} \begin{bmatrix} B_{ix} \\ B_{iy} \end{bmatrix}, \tag{4}$$

where $\mathbf{p} = [x, y]^{\mathbf{T}}$, $\mathbf{r} = [\phi]^{\mathbf{T}}$.

As such, the mapping between the pose $\mathbf{x} = [\mathbf{p}^{\mathbf{T}} \mathbf{r}^{\mathbf{T}}]^{\mathbf{T}} \in \mathbb{R}^3$ of the flying platform in the operational space and the length of the cables $\parallel \mathbf{BA} \parallel \in \mathbb{R}^4$ in the configuration space is identified. It must be underlined that since the kinematic transmission functions comprise the variable $u_i$ for the "whole squad movement" stage of motion, the inverse kinematics procedure will not be straightforward, and the actuation redundancy leads to an under-constrained kinematic equation. However, this presence also allows us to optimize the cable tension distribution to satisfy certain desired criteria, which will be discussed in Section V-C.

In addition, kinematic singularities analysis is essential. In our case, an uncertainty singularity occurs when the four driving cables intersect at a single point; such a configuration is unavoidable given the base mobility. At this singular configuration, the axis perpendicular to the motion plane becomes uncontrollable, rendering the system unable to alter the rotational orientation of the flying platform due to the loss of torque authority in that degree of freedom. To compensate for this disadvantage, we introduce a rotational joint at the end of the flying platform to control the yaw of the Euler angle of the flying platform in the mechanical design phase. With this DoF, the flying gripper can liberally adjust to the optimal angle to align with the inclination angle of the stay cable to be grasped. Consequently, altering the flying platform's rotational orientation does not require any adjustment of the tension distribution of the driving cables.

**Dynamics** For a given pose of the flying platform, we need to consider the force and torque equilibrium to achieve static stabilization. All forces and torques acting on the flying platform can be expressed as

$$\begin{cases} \sum_{i=1}^{4} \mathbf{f}_i + \mathbf{f}_p = 0 \\ \sum_{i=1}^{4} {}^{l}\mathbf{B}_i \times \mathbf{f}_i + \boldsymbol{\tau}_p = 0 \end{cases}, \tag{5}$$

where $\mathbf{w}_p = [\mathbf{f}_p, \boldsymbol{\tau}_p]^{\mathbf{T}} \in \mathbb{R}^3$ is the wrench applied on the flying platform, and $\mathbf{f}_i$ represents the tension force along the driving cable. Let $\mathbf{f}_i = f_i \mathbf{BA}_i / \parallel BA_i \parallel$, $\mathbf{f} = [f_1, f_2, f_3, f_4]^{\mathbf{T}}$ and substituting them into Eq. (5) leads to the following linear system:

$$\begin{bmatrix} \frac{\mathbf{BA}_1(u_1)}{\|\mathbf{BA}_1(u_1)\|} & \cdots & \frac{\mathbf{BA}_4(u_4)}{\|\mathbf{BA}_4(u_4)\|} \\ {}^{l}\mathbf{B}_1 \times \frac{\mathbf{BA}_1(u_1)}{\|\mathbf{BA}_1(u_1)\|} & \cdots & {}^{l}\mathbf{B}_4 \times \frac{\mathbf{BA}_4(u_4)}{\|\mathbf{BA}_4(u_4)\|} \end{bmatrix} \begin{bmatrix} f_1 \\ f_2 \\ f_3 \\ f_4 \end{bmatrix} + \begin{bmatrix} \mathbf{f}_p \\ \boldsymbol{\tau}_p \end{bmatrix} = 0, \tag{6}$$

where $\times$ refers to the cross-product operation and $\parallel \mathbf{BA}_i(u_i) \parallel$ is the Euclidian second norm of $\mathbf{BA}_i$ representing the cable $i$ length. To this end, we can abbreviate Eq. (6) in a compact matrix-vector form as

$$\mathbf{J}(\mathbf{x}, \mathbf{q}(\mathbf{u}))^{\mathbf{T}} \mathbf{f} + \mathbf{w}_p = 0, \tag{7}$$

where $\mathbf{J}(\mathbf{x}, \mathbf{q}(\mathbf{u})) \in \mathbb{R}^{4\times 3}$ is the joint space *Jacobian* of CCRobot-S, $\mathbf{q}(\mathbf{u}) = [u_1, u_2, u_3, u_4]^{\mathbf{T}}$. As such, we can see that the joint space *Jacobian* depends on the pose of the flying platform $\mathbf{x}$ and the reconfigurable positions of the movable anchor bases $\mathbf{q}(\mathbf{u})$.

The application of Newton-Euler formalism yields the equation of motion of CCRobot-S

$$\mathbf{M}(\mathbf{x})\ddot{\mathbf{x}} + \mathbf{C}(\mathbf{x}, \dot{\mathbf{x}})\dot{\mathbf{x}} + \mathbf{g}(\mathbf{x}) + \mathbf{w}_{ext} = \mathbf{J}(\mathbf{x}, \mathbf{q}(\mathbf{u}))^{\mathbf{T}} \mathbf{f}, \tag{8}$$

where $\mathbf{M}(\mathbf{x}) \in \mathbb{R}^{3\times 3}$ is the mass inertia matrix, $\mathbf{C}(\mathbf{x}, \dot{\mathbf{x}})\dot{\mathbf{x}}$, $\mathbf{g}(\mathbf{x})$, $\mathbf{w}_{ext} \in \mathbb{R}^3$ are the Coriolis and centrifugal vector, the gravity and external wrench such as wind effect applied to the flying platform, respectively. It is worth noting that when the variables $u_i$ are constant, Eqs. (7) and (8) are the equations of motion for the "body movement" stage of motion of CCRobot-S. More specifically, the "body movement" stage of motion is a particular status of the "whole squad movement" stage in CCRobot-S.

## IV. WORKSPACE ANALYSIS

To determine the motion and climbing strategy of CCRobot-S, the reachable climbing workspace on the stay cables plane should be identified. In this work, to simplify the analysis process, we assume that the movable anchor base can firmly anchor on the stay cable, i.e., it can maintain its position and sustain positive cable tensions against any external wrench applied to or resisted by the flying platform, thereby ensuring continuous controllability of the flying platform. As such, we focus on achieving wrench closure, emphasizing the geometric parameters of CCRobot-S - i.e., the locations of the cable attachment points on the movable anchor bases and on the flying platform, as well as the pose of the flying platform. We adopt the wrench-closure workspace to evaluate CCRobot-S' translational and rotational abilities. The primary constraint and crucial criterion for the size and shape of the wrench-closure workspace is the necessity for maintaining positive cable tension for every driving cable. Since the number of cable actuators exceeds the degrees of freedom of the flying platform, the joint space *Jacobian* is not square, resulting in an under-determined and infinite solution for the tension distribution in the motion equation. Sophisticated analyses are required for the wrench-closure condition based on the motion equation (7). In such cases, the Moore-Penrose pseudo-inverse can be used to provide a general solution for Eq. (7) as follows:

$$\mathbf{f} = -\mathbf{J}(\mathbf{x},\mathbf{q}(\mathbf{u}))^{\mathbf{T}^{\dagger}}\mathbf{w}_p + Null(\mathbf{J}(\mathbf{x},\mathbf{q}(\mathbf{u}))^{\mathbf{T}})\lambda, \tag{9}$$

where $\mathbf{J}(\mathbf{x},\mathbf{q}(\mathbf{u}))^{\mathbf{T}^{\dagger}} = \mathbf{J}(\mathbf{x},\mathbf{q}(\mathbf{u}))(\mathbf{J}(\mathbf{x},\mathbf{q}(\mathbf{u}))^{\mathbf{T}}\mathbf{J}(\mathbf{x},\mathbf{q}(\mathbf{u})))^{-1}$ is the Moore-Penrose pseudo-inverse of $\mathbf{J}(\mathbf{x},\mathbf{q}(\mathbf{u}))^{\mathbf{T}}$, $Null(\mathbf{J}(\mathbf{x},\mathbf{q}(\mathbf{u}))^{\mathbf{T}})$ is the one-dimensional basis of the null space of $\mathbf{J}(\mathbf{x},\mathbf{q}(\mathbf{u}))^{\mathbf{T}}$. The first term on the right-hand side of Eq. (9) is the particular solution. The second term is the homogeneous solution, which projects an arbitrary vector $\lambda$ into the null space of $\mathbf{J}(\mathbf{x},\mathbf{q}(\mathbf{u}))^{\mathbf{T}}$. It is worth noting that the particular and homogeneous solutions are perpendicular to each other. The arbitrary vector $\lambda$ can shift all cable forces into other regions while not changing the original system of equations. Checking the wrench-closure workspace is a major challenge for the degrees of freedom actuation redundancy (r > 0) system (where r equals the number of driving cables m minus the number of degrees of freedom n). In this work, thanks to the degree of redundancy $r = 1$, $\lambda$ is a scalar parameter in this case. We can neglect the value of the applied wrench $\mathbf{w}_p$ since we can choose a sufficiently large $\lambda$ to ensure that the tension configuration renders all values positive, i.e., all cables keep pulling the flying platform. As a result, we can conclude that *iff* all the elements of $Null(\mathbf{J}(\mathbf{x},\mathbf{q}(\mathbf{u}))^{\mathbf{T}})$ have the same sign and are not equal to zero, a positive tension force distribution $\mathbf{f}$ exists, and the current pose of the flying platform belongs to the wrench-closure workspace, the mathematical deduction for the conclusion is given in Appendix B in detail.

For $\mathbf{J}(\mathbf{x},\mathbf{q}(\mathbf{u}))^{\mathbf{T}} = [\mathbf{J}_1(\mathbf{x},u_1)\ \mathbf{J}_2(\mathbf{x},u_2)\ \mathbf{J}_3(\mathbf{x},u_3)\ \mathbf{J}_4(\mathbf{x},u_4)]$, the null space vector can be labeled as $Null((\mathbf{J}(\mathbf{x},\mathbf{q}(\mathbf{u}))^{\mathbf{T}}) = [\mathbf{J}_1(\mathbf{x},\hat{u}_1)\quad \mathbf{J}_2(\mathbf{x},\hat{u}_2)\quad \mathbf{J}_3(\mathbf{x},\hat{u}_3)\quad \mathbf{J}_4(\mathbf{x},\hat{u}_4)]^{\mathbf{T}}$. The $i$th component of $Null((\mathbf{J}(\mathbf{x},\mathbf{q}(\mathbf{u}))^{\mathbf{T}})$, namely $\mathbf{J}_i(\mathbf{x},\hat{u}_i)$ $= (-1)^{i+1}det[\mathbf{J}_1(\mathbf{x},u_1)\ \ldots\ \mathbf{J}_{i-1}(\mathbf{x},u_{i-1})\ \mathbf{J}_{i+1}(\mathbf{x},u_{i+1})\ \ldots\ \mathbf{J}_4(\mathbf{x},u_4)]$, $i = 1,2,3,4$, $det_i$ is the determinant of the square matrix obtained from the matrix $\mathbf{J}(\mathbf{x},\mathbf{q}(\mathbf{u}))^{\mathbf{T}}$ by deleting its $i$th column. The expression of the one-dimensional basis of the null space of $\mathbf{J}(\mathbf{x},\mathbf{q}(\mathbf{u}))^{\mathbf{T}}$ is given in Eq. (10) and is derived and proved particularly in Appendix A.

$$Null(\mathbf{J}^{\mathbf{T}}) = \begin{bmatrix} +det\,[\mathbf{J}_2(\mathbf{x},u_2)\ \mathbf{J}_3(\mathbf{x},u_3)\ \mathbf{J}_4(\mathbf{x},u_4)] \\ -det\,[\mathbf{J}_1(\mathbf{x},u_1)\ \mathbf{J}_3(\mathbf{x},u_3)\ \mathbf{J}_4(\mathbf{x},u_4)] \\ +det\,[\mathbf{J}_1(\mathbf{x},u_1)\ \mathbf{J}_2(\mathbf{x},u_2)\ \mathbf{J}_4(\mathbf{x},u_4)] \\ -det\,[\mathbf{J}_1(\mathbf{x},u_1)\ \mathbf{J}_2(\mathbf{x},u_2)\ \mathbf{J}_3(\mathbf{x},u_3)] \end{bmatrix}, \tag{10}$$

where $\mathbf{J}(\mathbf{x},\mathbf{q}(\mathbf{u}))^{\mathbf{T}}$ is abbreviated as $\mathbf{J}^{\mathbf{T}}$.

Consequently, we can identify and quantify the wrench-closure workspace through an analytical expression Eq. (11) based on the same sign property for the elements of $Null(\mathbf{J}(\mathbf{x},\mathbf{q}(\mathbf{u}))^{\mathbf{T}})$.

$$\mathcal{W} = \left\{ \mathbf{p}^{\mathbf{T}} \in \mathbb{R}^2, \mathbf{r}^{\mathbf{T}} \in SO_1 \;\middle|\; \begin{matrix} \mathbf{J}_1(\mathbf{x},\hat{u}_1)\mathbf{J}_2(\mathbf{x},\hat{u}_2) > 0 \\ \mathbf{J}_1(\mathbf{x},\hat{u}_1)\mathbf{J}_3(\mathbf{x},\hat{u}_3) > 0 \\ \mathbf{J}_1(\mathbf{x},\hat{u}_1)\mathbf{J}_4(\mathbf{x},\hat{u}_4) > 0 \end{matrix} \right\}. \tag{11}$$

Apart from the wrench-closure workspace identification and quantification, it is also crucial to characterize the quality of this workspace. In this work, we introduce the Tension Factor (TF) concept to measure and evaluate the quality of wrench closure. It is defined as the ratio between the smallest actual cable tension and the largest actual cable tension among all cable tensions. For the degree of freedom actuation redundancy system ($m - n = r > 0$), the tension distribution of the cables is, however, complicated since the redundant cables are employed to drive the object. The smallest and largest actual cable tensions are challenging to formulate analytically. For a system with redundancy in actuation for one degree of freedom ($m - n = 1$), the homogeneous solution of the cable tensions $Null(\mathbf{J}(\mathbf{x},\mathbf{q}(\mathbf{u}))^{\mathbf{T}})$ is a one-dimensional null space vector. Thus, if the movable anchor bases are fixed, the tension factor is unique for a given flying platform pose. Subsequently, we use the smallest and the largest null space component of the homogeneous solution to replace the smallest and largest actual cable tensions to calculate the tension factor at a given pose, as shown in Eq. (12), which is in closed analytical form, and the cable force is not involved.

$$\mathbf{TF}_j = \frac{\min\{Null(\mathbf{J}(\mathbf{x}_j,\mathbf{q}(\mathbf{u})_i)^{\mathbf{T}})\}}{\max\{Null(\mathbf{J}(\mathbf{x}_j,\mathbf{q}(\mathbf{u})_i)^{\mathbf{T}})\}}, \tag{12}$$

where $i$ is the configuration of the four movable anchor bases, and $j$ is the posture point of the flying platform in the wrench-closure workspace. $\mathbf{TF}_j$ is usually a local measure and evaluation of the tension distribution for a given pose $j$ of the flying platform under a special configuration $i$ of all movable anchor bases. To acquire the whole workspace performance index, the global maximum Tension Factor (*max* TF) and global mean Tension Factor (*mean* TF) are proposed to characterize the global tension index.

For the global maximum tension factor, we consider the maximum value in all the local TFs over the workspace as the objective function, i.e.:

$$\mathit{max}\ \mathbf{TF} = \max \frac{\min\{Null(\mathbf{J}(\mathbf{x},\mathbf{q}(\mathbf{u}))^{\mathbf{T}})\}}{\max\{Null(\mathbf{J}(\mathbf{x},\mathbf{q}(\mathbf{u}))^{\mathbf{T}})\}}. \tag{13}$$

For the global mean tension factor, we propose the objective function as follows:

$$\mathit{mean}\ \mathbf{TF} = \frac{\int_v \mathbf{TF}(\mathbf{J}(\mathbf{x},\mathbf{q}(\mathbf{u}))^{\mathbf{T}})dV}{\int_v dV}, \tag{14}$$

where $v$ represents the workspace volume, $\mathbf{TF}(\mathbf{J}(\mathbf{x},\mathbf{q}(\mathbf{u}))^{\mathbf{T}})$ represents the changing values of TF which are based on the transposition of the joint space *Jacobian* $\mathbf{J}(\mathbf{x},\mathbf{q}(\mathbf{u}))^{\mathbf{T}}$, i.e. the pose $\mathbf{x}$ of the flying platform and the configuration $\mathbf{q}(\mathbf{u})$ of the movable anchor bases. According to the generation characteristic and finiteness of the wrench-closure workspace, the *mean* TF can be expressed separately under the condition

**IEEE Transactions on Robotics (T-RO) paper, presented at ICRA 2026, Vienna, Austria. Cite as T-RO paper.**

TABLE III
PARAMETERS OF THE FIXED-BASED STAGE OF MOTION FOR CCROBOT-S MODEL

| **Parameter sheet** | | | |
|---|---|---|---|
| **Movable anchor base vector (cm)** | | **Flying platform vector (cm)** | |
| ${}^{g}\mathbf{A}_1$ | $[0\ 0]^T$ | ${}^{l}\mathbf{B}_1$ | $[-9.5\ \ -9.5]^T$ |
| ${}^{g}\mathbf{A}_2$ | $[40.24\ 40.45]^T$ | ${}^{l}\mathbf{B}_2$ | $[9.5\ \ -9.5]^T$ |
| ${}^{g}\mathbf{A}_3$ | $[-35.22\ 89.66]^T$ | ${}^{l}\mathbf{B}_3$ | $[9.5\ 9.5]^T$ |
| ${}^{g}\mathbf{A}_4$ | $[-62.44\ 62.44]^T$ | ${}^{l}\mathbf{B}_4$ | $[-9.5\ 9.5]^T$ |
| $\boldsymbol{\alpha}$ | 33.1° | $\boldsymbol{\beta}$ | 45° |
| **Origin location of {g} (cm)** | | $[0\ 0]^T$ | |

that the orientation of the flying platform is constant or varying in a region and can be calculated numerically,

$$\textit{mean } \mathbf{TF} = \begin{cases} \dfrac{\sum_{j=1}^{n} \mathbf{TF}(\mathbf{J}(\mathbf{p},\mathbf{q}(\mathbf{u}))^{\mathbf{T}})}{n} & \text{for } \phi \text{ constant} \\ \dfrac{\sum_{k=1}^{m}\sum_{j=1}^{n} \mathbf{TF}(\mathbf{J}(\mathbf{x},\mathbf{q}(\mathbf{u}))^{\mathbf{T}})}{m\cdot n} & \text{for } \phi \text{ varying} \end{cases}, \tag{15}$$

where $\mathbf{TF}(\mathbf{J}(\mathbf{p},\mathbf{q}(\mathbf{u}))^{\mathbf{T}})$ represents the values of TF calculated based on the translation $\mathbf{p}$ of the flying platform while the orientation $\mathbf{r}$: $\phi$ is constant, i.e., a constant orientation workspace. $\mathbf{TF}(\mathbf{J}(\mathbf{x},\mathbf{q}(\mathbf{u}))^{\mathbf{T}})$ represents the values of the TF calculated from every translation $\mathbf{p}_j$ and every orientation $\mathbf{r}_k$ of the flying platform, i.e. the varying orientation workspace, and $n$ is the number of points that constitute the constant orientation workspace, and $m$ is the number of points covering the range region of possible orientations.

Overall, the *max* TF and the *mean* TF are essential criteria and performance indices to evaluate the tension distribution and wrench closure property. A larger *max* TF or *mean* TF means the difference value between the minimum and maximum cable force is small. This is desirable since there is a better tension balance, which means that the cables can better strain the pose of the flying platform, and the system can remain stable against external disturbance. Additionally, a higher *max* TF or *mean* TF also means better manipulability and robustness of the flying platform. As such, *max* TF or *mean* TF is always considered and adopted as a performance criterion for task-based optimization problems to design an optimal system.

For the "body movement" stage of motion of CCRobot-S, the movable anchor bases will anchor on the stay cables, the variables $u_i$ are constant, and their values are given by the encoders, which are integrated on the wheels of the movable anchor bases. As such, the system is fixed-based, and the entire wrench-closure workspace and the global tension performance index (the TF values at every flying platform pose) can be calculated and derived through Eqs. (13) and (14). To clarify further, we present an example in which the four movable anchor bases are anchored, and their positions are known. The specific parameter sheet is given in Tab. III.

Fig. 8 illustrates the entire wrench-closure workspace of fixed-based CCRobot-S, collecting every point that the flying platform can reach and the counterpart's TF value under the wrench-closure condition with the flying platform's orientation $\phi = 50°$. It can be shown that the wrench-closure workspace is a subset of the region enclosed by the four movable anchor base points. When the TF approaches zero, i.e., at least one cable of CCRobot-S has only tiny tension, the flying platform is close to the workspace boundary. When the TF approaches 1, the flying platform is always located near the geometric center of the workspace. In this work, we also investigate the TF map when the orientation of the flying platform is changing (see Fig. 9). We can see that the workspace or the tension distribution changes drastically when adjusting the flying platform's orientation. The flying platform has certain desired orientation angles, where the system possesses desired kinematic characteristics. When the orientation angle deviates from the desired values, the kinematic characteristics of CCRobot-S will degenerate with workspace contraction, and the *max* TF value will decrease. Most TFs may not be favorable due to the unstable tension balance among the driving cables.

For the "whole squad movement" stage of motion of CCRobot-S, the movable anchor bases' locations are relocated, and the wrench-closure workspace or the counterpart's TF map of CCRobot-S is also changing according to Eqs. (13), (14) and (15). In this case, the elements of the transposition of the joint space *Jacobian* $\mathbf{J}(\mathbf{x},\mathbf{q}(\mathbf{u}))^{\mathbf{T}}$ for CCRobot-S are functions of reconfigurable variables $u_i$. Hereby, the wrench-closure workspace and its counterpart's TF are expressed analytically as multi-variable functions through Eqs. (11) and (12), which indicates the reconfiguration problem can be formulated into a multi-variable problem about $\mathbf{q}(\mathbf{u})$. The climbing strategy optimization for CCRobot-S in Section V is based on this analysis. When we set the values of variables $u_i$, the system of CCRobot-S translates into the "body movement" stage of motion of CCRobot-S. More specifically, the "whole squad movement" stage of motion of CCRobot-S is the iteration and combination of the "body movement" stage of motion of CCRobot-S. While this leads to the challenge of the theoretical derivation, actuation redundancy, and kinematics procedure, in turn, it offers the opportunity to achieve the benefits of workspace expansion, which has been elaborated in Section II-C, and performance improvement, which will be analyzed in depth with optimal design in Section V-C.

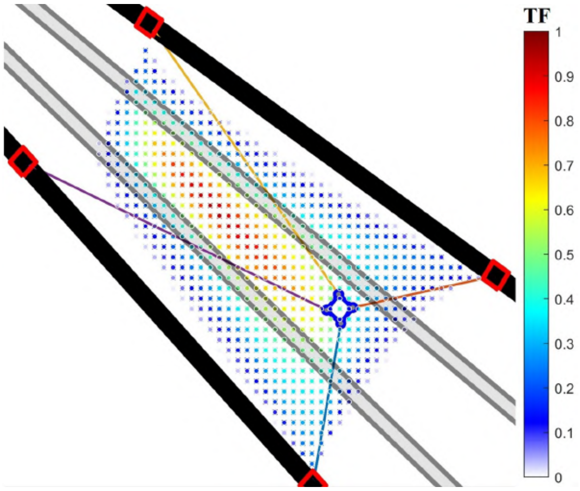

Fig. 8. Example of the constant orientation workspace and TF map for fixed-based CCRobot-S with flying platform's orientation $\phi = 50°$.

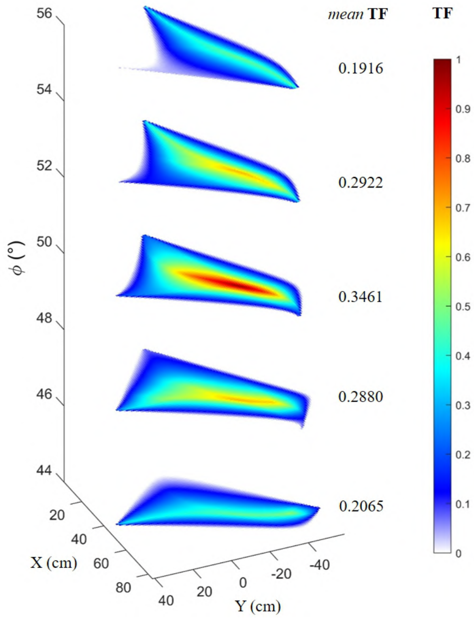

Fig. 9. Example of varying orientation workspace and TF map for fixed-based CCRobot-S where the flying platform's orientation $\phi$ shifts from 44° to 56°.

## V. CLIMBING STRATEGY AND OPTIMIZATION

Based on the CCRobot-S model and its workspace analysis, we can further analyze the climbing strategy and optimization for CCRobot-S. Since the general climbing strategy – the spider-like climbing gait and the zero-downtime climbing gait, which are task-based, have been illustrated in Section II-C, in this Section, we will delve into the climbing implementation strategy and optimization. First, an approach is proposed to meet the essential prerequisite for the successful maneuver of CCRobot-S: the stability of the movable anchor base. Then, the strategy for the motion of CCRobot-S is also presented. After that, the optimal control for the grasp arrangement and the anchor reconfiguration of CCRobot-S is discussed.

### *A. Gripper's Adhesion Approximation and Verification*

An essential prerequisite for the successful maneuver of CCRobot-S is that the movable anchor base can perch on the desired position of the stay cable stably without any deviation along the stay cable or rotation around the stay cable under the influence of environmental wrenches and the tension of the driving cables. As discussed, the formulation of the wrench-closure workspace and evaluation criteria is predicated on the assumption of a stable base. Any deviation from this stability could result in tension changes or cable sagging, leading to significant changes in the workspace and rendering the established evaluation criteria unsuitable for real-world scenarios.

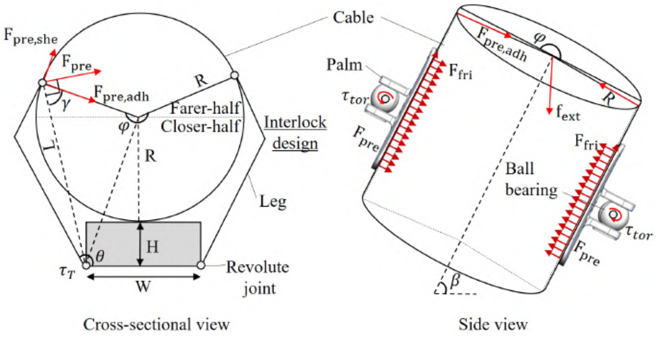

Fig. 10. Representation of the gripper anchoring on the stay cable.

To address this challenge, our team has developed a novel gripping module [14] to fasten the movable anchor base onto the stay cable surface, the transmission system for the power and the force analysis is exploited and introduced in [14]–[16]. Some modifications are introduced and discussed hereafter. Fig. 10 illustrates the simplified gripping module clamping on the stay cable. L is the length of the palm, and W denotes the distance between the two revolute joints of the palm. H represents the vertical distance between the revolute joint of the palm and the stay cable surface. R is the radius of the stay cable. The gripping force $\mathrm{F}_{\mathrm{pre}}$, which can generate both shear force $\mathrm{F}_{\mathrm{pre,\ she}}$ and adhesive force $\mathrm{F}_{\mathrm{pre,\ adh}}$, is generated by the compression between the palms and the stay cable surface as a function of the joint torque $\boldsymbol{\tau}_T$. According to the force equilibrium,

$$2\mu \mathrm{F}_{\mathrm{pre}} \cos(90^\circ - \boldsymbol{\gamma}) \geq \mathrm{f}_{\mathrm{ext}} \sin \boldsymbol{\beta} \pm \mu \mathrm{f}_{\mathrm{ext}} \cos \boldsymbol{\beta}, \tag{16}$$

where $\boldsymbol{\gamma} = \arccos \frac{\mathrm{R}^2+\mathrm{L}^2-(\mathrm{R}+\mathrm{H})^2-(\frac{\mathrm{W}}{2})^2}{2\mathrm{RL}}$, $\mu$ is the friction coefficient, $\boldsymbol{\beta}$ is the inclination angle of stay cable, $\mathrm{f}_{\mathrm{ext}}$ is the external force which is summing of the gravity, the tension of the cable, and the environment force. Subsequently,

$$\mathit{min}\ \mathrm{F}_{\mathrm{pre}} = \frac{\mathrm{f}_{\mathrm{ext}}(\sin \boldsymbol{\beta} \pm \mu \cos \boldsymbol{\beta})}{2\mu \cos(90^\circ - \boldsymbol{\gamma})} \ . \tag{17}$$

By substituting $\boldsymbol{\gamma} = \arccos \frac{\mathrm{R}^2+\mathrm{L}^2-(\mathrm{R}+\mathrm{H})^2-(\frac{\mathrm{W}}{2})^2}{2\mathrm{RL}}$ into Eq. (17) with the constants: estimated external force $\mathrm{f}_{\mathrm{ext}}$ = 300 N, W = 0.12 m, H = 0.015 m, and $\mu$ = 0.3, the relationship map between the minimum gripper force $\mathrm{F}_{\mathrm{pre}}$, the radius of the stay cable R, and the inclination angle of the stay cable $\beta$ is further presented in Fig. 11. Given that the characteristic parameters of stay cables vary across different bridge structures, it is essential and convenient to approximate a suitable minimum gripper force for climbing based on this relationship mapping.

In addition, due to the imprecision of the force control caused by the self-locking nature of the worm gears equipped on the movable anchor base, a perceptive system for the gripper has been developed to detect pressure variations and unexpected unanchored states between the palms and cable

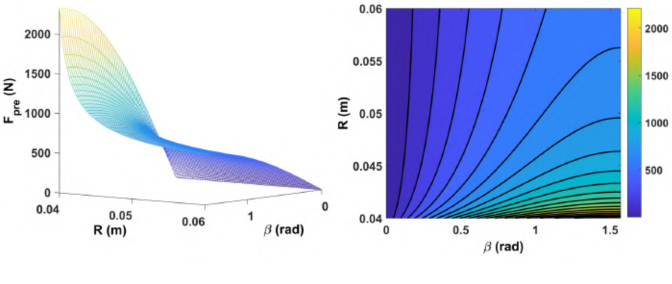

Fig. 11. Relationship map between the minimum gripper force and the characteristic parameters of the stay cable (left); R-$\beta$ plane projection of minimum gripper force $\mathrm{F}_{\mathrm{pre}}$ (right).

**IEEE Transactions on Robotics (T-RO) paper, presented at ICRA 2026, Vienna, Austria. Cite as T-RO paper.**

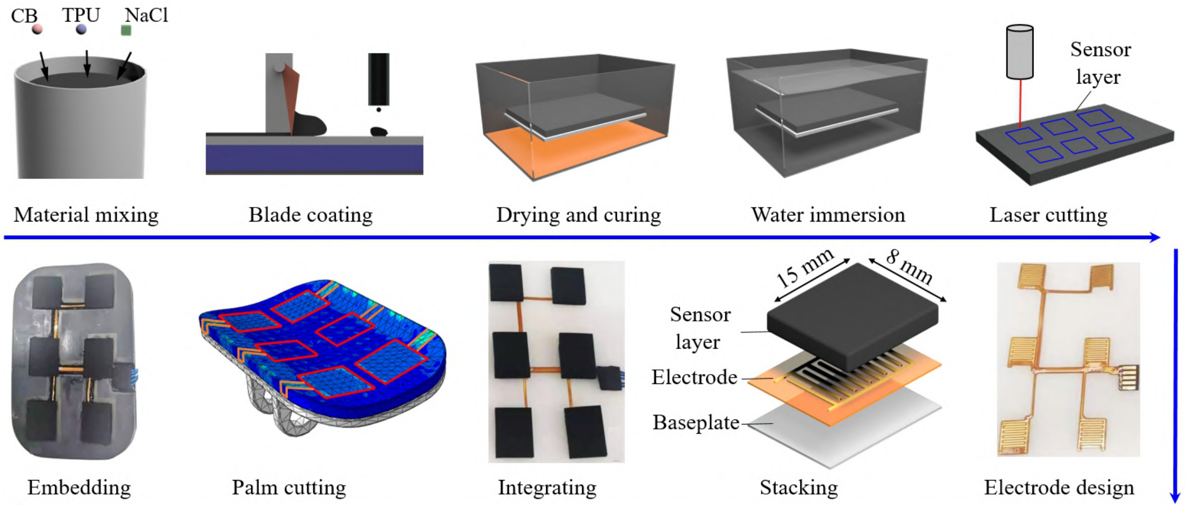

Fig. 12. Fabrication of the flexible hierarchical perceptive sensor embedded in the gripper's palm (*CB = Carbon Black, TPU = Thermoplastic Polyurethanes, NaCl = NaCl crystals).

surfaces. While conventional pressure sensors continuously improve their sensitivity, their response range is inherently limited by structural compressibility, especially under high loading forces. A flexible hierarchical perceptive sensor is designed and fabricated for effective sensing under large loading forces. It is embedded in the palm of the gripper and applied to improve the palm's sensing sensitivity while simultaneously broadening the pressure responding range. Fig. 12 shows how the perceptive palm is customized for the climbing scenario under high shear force conditions. With this sensor, the gripper can explore the cable surface and measure the adhesive force on different locations of the palm. According to the feedback of $F_{pre}$, the movable anchor bases can determine whether the palm is securely attached to the cable based on the predefined adhesion verification criteria as shown in Fig. 13.

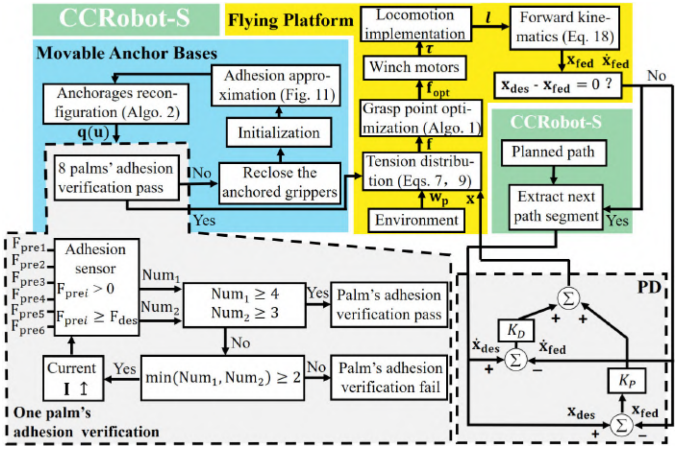

Fig. 13. Schematic of CCRobot-S' motion implementation.

## *B. Strategy for Motion Implementation of CCRobot-S*

After satisfying the essential prerequisite for the successful maneuver of CCRobot-S, the motion implementation of CCRobot-S is considered. The strategy framework is depicted in Fig. 13. First, the Cartesian position, the inclination angle, and the radius of the climbing stay cables, which are given in advance, are input for system initialization to approximate the required adhesion. The system then verifies the adhesion using the flexible hierarchical perceptive sensor on the palm. On top of that, the positions of the movable anchor bases: $\mathbf{q}(\mathbf{u})$ are monitored via encoders integrated into the wheels of the movable anchor bases. Based on that, we further analyze the motion implementation of the flying platform. To follow a planned trajectory and realize a desired motion under four synchronous driving cable tensions, we need to update the set point and the cable tensions every few milliseconds, which means the tension control operates at the kHz range. Our team adopts the virtual tension and *Jacobian* transposed control techniques to achieve high control frequencies, high bandwidth, and force sensing. This method involves measuring the winch motor torque through motor current and estimating the flying platform's wrench using cable tensions in conjunction with CCRobot-S' transposed *Jacobian* mapping $\mathbf{J}(\mathbf{x}, \mathbf{q}(\mathbf{u}))^{\mathbf{T}}$. To facilitate these operations, we choose a quasi-direct-drive actuator for the winch actuator, striking a balance between force transparency, mechanical impedance, torque density, and speed. The gear train features a low reduction of 9, ensuring accurate proprioceptive sensing while amplifying winch torque to propel the heavy-duty flying platform or withstand high-impact forces.

The position accuracy of the flying platform is also crucial to achieving the desired motion of the flying platform, as it significantly impacts the grasping effectiveness of the flying gripper. An inaccurate position of the flying platform could result in the flying gripper failing to grasp or anchor securely on the stay cable. Consequently, forward kinematics is introduced to estimate the pose and velocity of the flying platform as the feedback values, and a Proportional-Derivative (PD) feedback loop control is implemented.

However, solving the forward kinematics for cable-driven parallel mechanisms is rather intricate. In this work, we interpret solving the forward kinematics as an optimization problem. The cable lengths corresponding to the desired pose

**IEEE Transactions on Robotics (T-RO) paper, presented at ICRA 2026, Vienna, Austria. Cite as T-RO paper.**

of the flying platform are denoted as $\boldsymbol{l}_o$, while the cable lengths derived from the inverse kinematic model (Eq. (3)) by a given pose $\mathbf{x}$ are represented as $\boldsymbol{l}(\mathbf{x})$. The forward kinematics can be reformulated as an optimization task focused on minimizing the error between $\boldsymbol{l}_o$ and $\boldsymbol{l}(\mathbf{x})$. The objective function $\varsigma(\mathbf{x}) = \frac{1}{2} \parallel \boldsymbol{l}(\mathbf{x}) - \boldsymbol{l}_o\|_2^2$ is denoted by the Euclidean norm denoted as $\parallel \|_2$. The general formulation of the optimization problem is then

$$\begin{aligned} \mathbf{x}^* = \arg\min_{\mathbf{x}} \frac{1}{2} \parallel \boldsymbol{l}(\mathbf{x}) &- \boldsymbol{l}_o\|_2^2 \\ \text{s.t.} \quad \boldsymbol{l}(\mathbf{x}) &= \mathbf{BA}(\mathbf{x}) \\ \mathbf{TF}_{\mathbf{x}_g} &\geq const \\ \mathbf{x} &\in \mathcal{W} \end{aligned}, \tag{18}$$

where $\mathbf{BA}(\mathbf{x}) = [\mathbf{BA}_1(\mathbf{x}), \mathbf{BA}_2(\mathbf{x}), \mathbf{BA}_3(\mathbf{x}), \mathbf{BA}_4(\mathbf{x})]^{\mathbf{T}}$, $\mathbf{BA}_i(\mathbf{x})$ can be derived from Eq. (4), and $u_i$ are constant in this case. $\mathbf{x}_g$ denotes the initial guess pose, $\mathbf{TF}_{\mathbf{x}_g}$ can be calculated through Eq. (12), $\mathcal{W}$ signifies the current wrench-closure workspace under a specific configuration, defined in Eq. (11).

In this process, the variable $\mathbf{x}$ is constrained by the boundary of the workspace, $\mathbf{x}_g$ is determined by a preset TF constant value $const$, which is set close to 1, initiating the iterative optimization from the geometric center of the workspace. With these constrained functions and limit ranges of the variable for the quadratic cost function, the proposed strategy ensures convergence, ultimately identifying a precise solution $\mathbf{x}^*$.

### C. *Optimization*

In this study, two kinds of task-based optimization problems are formulated to meet certain criteria: one is the optimal control for the grasp arrangement when the flying gripper needs to fasten onto the stay cable. This strategy, termed grasp arrangement optimization, is proposed for stay cable maintenance; the other is the optimal control for the cable attachment reconfiguration of the movable anchor bases when the flying platform follows a planned trajectory. This strategy, termed anchor reconfiguration optimization, is proposed for stay cable inspection. It is important to note that the grasp arrangement optimization problem is independent and isolated from the anchor reconfiguration optimization problem. The grasp arrangement optimization problem typically arises in the spider-like climbing gait, while the anchor reconfiguration optimization problem arises in the zero-downtime climbing gait. For the joint space *Jacobian* $\mathbf{J}(\mathbf{x}, \mathbf{q}(\mathbf{u}))$, $\mathbf{q}(\mathbf{u})$ is assumed to be fixed in the grasp arrangement optimization analysis, and $\mathbf{x}$ is supposed to be fixed or follow a given trajectory in the anchor reconfiguration optimization analysis.

**Grasp Arrangement Optimization** For stay cable maintenance, the flying platform needs to attach itself to the stay cables to endure the dynamic loads and impacts from grinding, cleaning, or repair processes. Before grasping, the flying gripper needs to be maneuvered to approach the stay cable and rotate its orientation to hold on to the stay cable. Therefore, determining the optimal grasping position requires evaluating the stiffness and manipulability of the flying platform under cable tensions. As aforementioned, maximizing the TF enhances the manipulability and robustness of the flying platform. As a result, we use *max* TF as the objective function. For stay cable grasping, there is an intuitive constraint parallelogram region. This region has two parallel sides perpendicular to the stay cable to be grasped and two parallel sides parallel to the stay cable, defining a set of desired grasping points. The constraint parallelogram region is expressed as:

$$\mathcal{S} = \left\{ \mathbf{p} \in \mathbb{R}^2, \mathbf{r} \in SO_1 \left| \begin{aligned} &F_1(x,y) = y - (ax+b) \leqslant \delta \\ &F_2(x,y) = y - (ax+b) \geqslant -\delta \\ &F_3(x,y) = y - (-\frac{x}{a} + c) \leqslant \bar{\varepsilon} \\ &F_4(x,y) = y - (-\frac{x}{a} + c) \geqslant \underline{\varepsilon} \end{aligned} \right. \right\}, \tag{19}$$

where $y = ax + b$ is the central axis of the stay cable to be grasped, the constant coefficients $\delta$ and $\varepsilon$ formulate the constraint parallelogram region collecting the desired grasping points. As a result, the set $\mathcal{C}$ collecting the comprehensive positions is given by the intersection region,

$$\mathcal{C} = \mathcal{S} \cap \mathcal{W}, \tag{20}$$

and the optimal grasp arrangement searches for the desired point that corresponds to the *max* TF under the constraint of $\mathcal{C}$.

This study employs a recursive algorithm to search for the optimal grasping point, as outlined in Algorithm 1, which presents the pseudo-code for generating the optimal grasp arrangement. This algorithm leverages the properties of the wrench-closure workspace regions, characterized by varying TF values from high to low, to approach the desired parallelogram region. The intersection of these regions forms a set containing the desired grasp points. By ensuring a sufficiently small constant $\epsilon$, the intersection may encompass points sharing the same maximum TF values. Among these points, the algorithm evaluates the vertical distance $d_i$ from each point $\mathbf{x}_i$ to the center axis of the stay cable represented by $y = ax + b$ to identify the optimal grasp point. A smaller vertical distance indicates that the flying gripper is closer to the center axis of the stay cable, enhancing grasping performance. Therefore, the optimal grasp point is determined as the point within the intersection possessing the minimum vertical distance. Building upon the example in Section IV, the process of the searching algorithm is shown in Fig. 14, and the implementation of the algorithm to search for the optimal grasp point is found to be efficient.

This optimization analysis focuses on the position $\mathbf{p}$ of the flying gripper in Eqs. (11) and (19) while omitting consideration of the rotation $\mathbf{r}$ of the flying gripper due to its limited controllability and adjustability, as discussed in Section IV. Adjusting the orientation angle of the flying platform impacts the tension distribution significantly, leading to workspace contraction and a decrease in the maximum TF values. In practice, the desired range of orientation angles is typically narrow. To compensate for this disadvantage, we introduce a rotational joint on the end of the flying platform to control the yaw of the Euler angle of the flying gripper in the mechanical design phase, as illustrated in Fig. 3. With this DoF, the flying gripper can liberally adjust to the optimal angle to align with

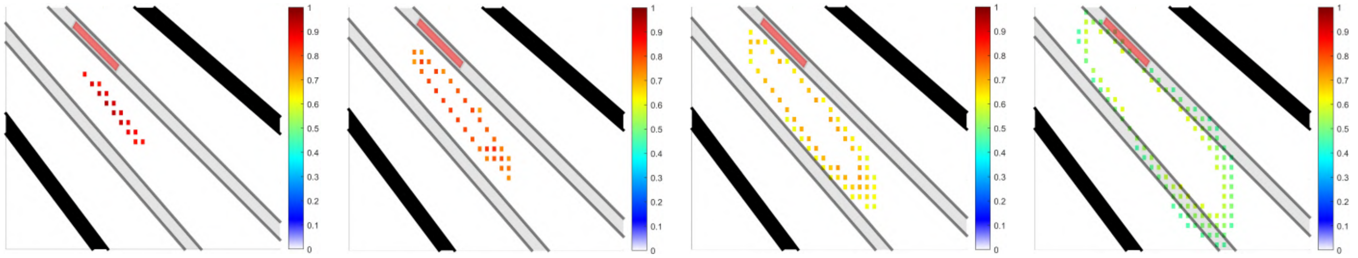

Fig. 14. Schematic of the process of the search algorithm for the optimal grasp point. In this diagram, the light red box indicates the desired parallelogram region to be grasped, and the grey and black boxes present the stay cables. TF values are changing from high to low $((0.85-1) \rightarrow (0.725-0.85) \rightarrow (0.6-0.725) \rightarrow (0.45-0.6))$ to implement the algorithm.

the inclination angle of the stay cable to be grasped without altering the tension distribution of the driving cables.

**Algorithm 1:** Generation of the Optimal Grasp Arrangement

```
Input: Movable anchor bases' position $\mathbf{q}(\mathbf{u})$,
       parallelogram region $\mathcal{S}$
Output: The pose of the desired point to be grasped
        for the flying platform
initialization;
$\mathcal{W} \leftarrow$in (11);
$\mathcal{C} \leftarrow$in (20);
$\kappa = 1$;
while 1 do
    $\mathcal{T} \leftarrow$ max TF in (13) $\geq \kappa - \epsilon$;
    $\kappa = \kappa - \epsilon$;
    $\mathcal{O} = \mathcal{T} \cap \mathcal{C}$;
    if $\mathcal{O} \neq \emptyset$ then
        go to next section;
    else
        go back to the beginning of the current section;
    end
end
$\mathcal{O} = \{\mathbf{x}_1, \mathbf{x}_2, ...\mathbf{x}_z\}$;
for $i \leftarrow 1$ to $z$ do
    $d_i = \frac{|ax_i - y_i + b|}{\sqrt{a^2+1}}$;
end
min $d_i = \min\{d_1, d_2, ...d_z\}$;
$\mathbf{x}_{des} \leftarrow$ min $d_i$
```

**Anchor Reconfiguration Optimization** For the stay cable inspection, the flying platform is typically equipped with a high-definition camera to navigate along the stay cable surface. Therefore, maintaining the stability of the flying platform is crucial to ensure the quality of captured images, mitigating issues such as shaking or defocusing. A higher TF contributes to the flying platform's stability, rigidity, and robustness. Thus, as discussed above, in the anchor reconfiguration optimization problem, TF is utilized as the performance evaluation metric under the wrench-closure condition. Anchor reconfiguration optimization optimizes TF for stability at every pose along a planned trajectory by reconfiguring the cable attachment locations on the movable anchor bases. Although the reconfiguration mechanism and actuation redundancy complicate the robotic system, they allow us to optimize the TF.

In this situation, since the movable anchor bases are restrained on the stay cables, the reconfiguration path for each reconfigurable attachment point is a one-dimensional motion, and the location of each attachment point can be described by a parametric polynomial function with the variable $u_i$,

$$ {}^{g}\mathbf{A}_i(u_i) = [A_{ix}(u_i) \quad A_{iy}(u_i)]^{\mathbf{T}}; \; i = 1,2,3,4, \tag{21} $$

where $u_{i,\min} \leq u_i \leq u_{i,\max}$. Furthermore, each cable segment can be expressed by substituting Eq. (21) into Eqs. (3) and (4), each reconfigurable cable is also a parametric function concerning the variable $u_i$. As a result, the anchor reconfiguration optimization problem can be formulated into a multi-variable optimization problem, aiming to maximize the TF at each pose along a given trajectory. This study proposes a hybrid approach to lower computational complexity and enhance optimization efficiency. This approach combines analytical formulations with numerical methods to identify the optimal configuration. The constraint condition, namely the wrench-closure workspace, can be explicitly expressed as polynomial inequalities, allowing for analytical treatment. On the other hand, the objective of maximizing TF necessitates a numerical solution through iterative methods, where each variable is discretely adjusted within the range of interest. Since the constraint condition in Eq. (11) is a set of multi-variable inequalities, which are not polynomials due to the presence of the denominator of the stay cable lengths $\parallel \mathbf{BA} \parallel$ in $\mathbf{J}(\mathbf{x}, \mathbf{q}(\mathbf{u}))^{\mathbf{T}}$. To eliminate the denominator, we introduce $\tilde{\mathbf{J}}(\mathbf{x}, \mathbf{q}(\mathbf{u}))^{\mathbf{T}} = \mathbf{J}(\mathbf{x}, \mathbf{q}(\mathbf{u}))^{\mathbf{T}} \cdot diag(\parallel \mathbf{BA}_1 \parallel, ..., \parallel \mathbf{BA}_4 \parallel)$ to replace the term $\mathbf{J}(\mathbf{x}, \mathbf{q}(\mathbf{u}))^{\mathbf{T}}$. This transformation is valid since the cable lengths are strictly positive and do not affect the wrench-closure condition. Additionally, considering $\mathbf{x}$ as a given trajectory, it can be treated as a constant for each pose on the trajectory. As a result, we can rewrite the transposition of the joint space *Jacobian* as

$$ \tilde{\mathbf{J}}(\mathbf{q}(\mathbf{u}))^{\mathbf{T}} = \begin{bmatrix} \tilde{j}_{11}(u_1) & \tilde{j}_{21}(u_2) & \tilde{j}_{31}(u_3) & \tilde{j}_{41}(u_4) \\ \tilde{j}_{12}(u_1) & \tilde{j}_{22}(u_2) & \tilde{j}_{32}(u_3) & \tilde{j}_{42}(u_4) \\ \tilde{j}_{13}(u_1) & \tilde{j}_{23}(u_2) & \tilde{j}_{33}(u_3) & \tilde{j}_{43}(u_4) \end{bmatrix}. \tag{22} $$

In the following analysis, we will use $\tilde{\mathbf{J}}(\mathbf{q}(\mathbf{u}))^{\mathbf{T}}$ as the transposition of the joint space *Jacobian* to replace the term $\mathbf{J}(\mathbf{x}, \mathbf{q}(\mathbf{u}))^{\mathbf{T}}$. Based on that, according to the definition of the determinant,

$$ \tilde{\mathbf{J}}_i(\hat{u_i}) = \sum_{\sigma \in S_n} \mathrm{sgn}(\sigma) \tilde{j}_{1\sigma}(u_1) \cdots \tilde{j}_{n\sigma}(u_n), \tag{23} $$

where $S_n$ is the permutation group on the set $\{1, 2, ..., n\}$, $sgn(\sigma)$ is the parity of the permutation $\sigma$. We can observe that the component of the null space vector $Null(\tilde{\mathbf{J}}(\mathbf{q}(\mathbf{u}))^{\mathbf{T}})$ is the dot product of the elements in the matrix $\tilde{\mathbf{J}}(\mathbf{q}(\mathbf{u}))^{\mathbf{T}}$, which are either constant values or polynomials. Consequently, the solutions for the wrench-closure condition in Eq. (11) are a set of multi-variable polynomial inequalities.

**Algorithm 2:** Generation of the Optimal Anchor Configuration

```
Input: The poses of the flying platform
       $\mathbf{x}_j$ $(j = 1, 2, ..., n)$ on a given trajectory,
       $\mathcal{R} = \{\mathbf{q}(\mathbf{u}) : \mathbf{q}(\mathbf{u})_{\min} \leqslant \mathbf{q}(\mathbf{u}) \leqslant \mathbf{q}(\mathbf{u})_{\max}\}$,
Output: The locations of the desired points to be
        anchored for the movable anchor bases
initialization;
for $j \leftarrow 1$ to $n$ do
    $\mathbf{x}_j$ = $[\mathbf{p}_j^{\mathbf{T}} \mathbf{r}_j^{\mathbf{T}}]^{\mathbf{T}}$ ;
    loop=0;
    for $u_1 \in \mathcal{R}_1 \leftarrow u_{1\,\min}$ to $u_{1\,\max}$ do
        for $u_2 \in \mathcal{R}_2 \leftarrow u_{2\,\min}$ to $u_{2\,\max}$ do
            for $u_3 \in \mathcal{R}_3 \leftarrow u_{3\,\min}$ to $u_{3\,\max}$ do
                for $u_4 \in \mathcal{R}_4 \leftarrow u_{4\,\min}$ to $u_{4\,\max}$ do
                    $\tilde{\mathbf{J}}(\mathbf{q}(\hat{\mathbf{u}})) \leftarrow$ in (25);
                    TF $\leftarrow$ in (12);
                    $\mathcal{W}$ $\leftarrow$in (11);
                    if $\mathbf{x}_j \in \mathcal{W}$ then
                        loop=loop+1;
                        $k$=loop;
                        TF$_k$=TF;
                    else
                        loop=loop;
                    end
                end
            end
        end
    end
    max TF$_j$ = $\max\{\mathbf{TF}_1, \mathbf{TF}_2, ...\mathbf{TF}_k\}$;
    $\mathbf{q}(\mathbf{u})_j \leftarrow$ max TF$_j$;
end
$\mathbf{Q}(\mathbf{u}) = \{\mathbf{q}(\mathbf{u})_1, \mathbf{q}(\mathbf{u})_2, ..., \mathbf{q}(\mathbf{u})_j\}$
```

Finally, we can express the generic form to formulate the optimal configuration of CCRobot-S as:

$$\begin{aligned} \mathbf{q}(\mathbf{u})^* = \arg\max_{\mathbf{q}(\mathbf{u})} & \frac{\min\{Null(\tilde{\mathbf{J}}(\mathbf{q}(\hat{\mathbf{u}})))\}}{\max\{Null(\tilde{\mathbf{J}}(\mathbf{q}(\hat{\mathbf{u}})))\}} \\ \text{s.t.} \quad & \tilde{\mathbf{J}}_1(\hat{u_1}) \cdot \tilde{\mathbf{J}}_2(\hat{u_2}) > 0 \\ & \tilde{\mathbf{J}}_1(\hat{u_1}) \cdot \tilde{\mathbf{J}}_3(\hat{u_3}) > 0 \\ & \tilde{\mathbf{J}}_1(\hat{u_1}) \cdot \tilde{\mathbf{J}}_4(\hat{u_4}) > 0 \\ & \mathbf{q}(\mathbf{u})_{\min} \leqslant \mathbf{q}(\mathbf{u}) \leqslant \mathbf{q}(\mathbf{u})_{\max} \end{aligned}, \tag{24}$$

where the $\mathbf{q}(\mathbf{u})_{\min}$ and $\mathbf{q}(\mathbf{u})_{\max}$ represent the limits of the reconfigurable position for the movable anchor bases. The objective and constraint functions are multi-variable functions concerning the reconfigurable elements $u_i$. $Null(\tilde{\mathbf{J}}(\mathbf{q}(\hat{\mathbf{u}})))$ is the basis for the null space of $\tilde{\mathbf{J}}(\mathbf{q}(\mathbf{u}))^{\mathbf{T}}$, and it can be written as:

$$Null(\tilde{\mathbf{J}}(\mathbf{q}(\hat{\mathbf{u}}))) = [\tilde{\mathbf{J}}_1(\hat{u_1}) \ \tilde{\mathbf{J}}_2(\hat{u_2}) \ \tilde{\mathbf{J}}_3(\hat{u_3}) \ \tilde{\mathbf{J}}_4(\hat{u_4})]^{\mathbf{T}}. \tag{25}$$

The pseudo-code for generating the optimal anchorages is presented in Algorithm 2. This algorithm simplifies the search method for a given pose $\mathbf{x}$ by reducing the objective function with a single anchor pose variable while treating the remaining three variables as constants. These constants are iteratively adjusted within the limits of the movable cable attachment pose. This approach allows us to determine the maximum TF and evaluate if the current flying platform poses lie within the wrench-closure workspace defined by the polynomial inequalities under the current configuration. If the evaluation is successful, the optimization algorithm proceeds to the next pose along the given trajectory.

To study the reconfiguration mechanisms and validate the optimization effect, we still use the parameter sheet in Tab. III of Section IV as the initial conditions, and the reconfiguration profiles for the movable anchor bases are listed in Eq. (26), and the coordinates for the movable attachments are listed in Eq. (27).

$$\begin{matrix} -5 \leq s_1 - u_1 \cos\beta \leq 5 \\ -5 \leq s_2 - u_2 \cos\alpha \leq 5 \\ -5 \leq s_2 - u_3 \cos\alpha \leq 5 \\ -5 \leq s_1 - u_4 \cos\beta \leq 5 \end{matrix} ; u_1, u_2, u_3, u_4 \geq 0. \tag{26}$$

$$\begin{aligned} {}^g\mathbf{A}_1 &= \begin{bmatrix} s_1 - u_1 \cos\beta \\ -\tan(\beta)(s_1 - u_1 \cos\beta) + \tan(\beta) s_1 \end{bmatrix} \\ {}^g\mathbf{A}_2 &= \begin{bmatrix} s_2 - u_2 \cos\alpha \\ -\tan(\alpha)(s_2 - u_2 \cos\alpha) + \tan(\alpha) s_2 \end{bmatrix} \\ {}^g\mathbf{A}_3 &= \begin{bmatrix} s_2 - u_3 \cos\alpha \\ -\tan(\alpha)(s_2 - u_3 \cos\alpha) + \tan(\alpha) s_2 \end{bmatrix} \\ {}^g\mathbf{A}_4 &= \begin{bmatrix} s_1 - u_4 \cos\beta \\ -\tan(\beta)(s_1 - u_4 \cos\beta) + \tan(\beta) s_1 \end{bmatrix} \end{aligned} . \tag{27}$$

For the flying platform, the given trajectory of the task space is expressed by $\mathbf{x}(t) \in \mathbb{R}^3$ as shown in Eq. (28) with the time variable $0 \leq t \leq 50$ s, a linear motion is used based on the task that the flying platform is traveling along the stay cable.

$$\mathbf{x}(t) = \begin{bmatrix} 2 - t, & 0.8693t + 23.7107, & 49^\circ \end{bmatrix}^{\mathbf{T}}. \tag{28}$$

As a result, four types of reconfiguration mechanisms categorized by the number of movable anchor bases involved in the reconfiguration process are studied as shown in Fig. 15. The results indicate a substantial increase in the TF of the flying platform with anchor reconfiguration optimization, signifying an enhancement in the performance of the flying platform. Furthermore, the analysis reveals that the optimization effect improves with the increased involvement of movable anchor bases in the morphological optimization of the CCRobot-S system.

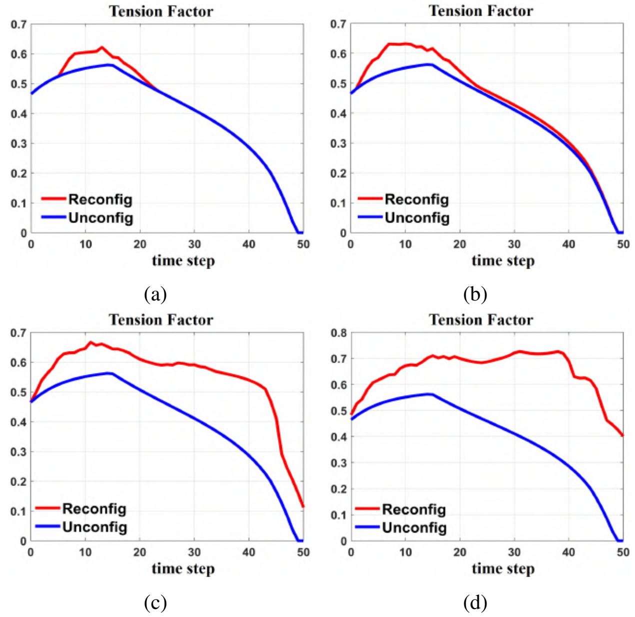

(a) (b) (c) (d)

Fig. 15. Performance improvement of the flying platform in terms of TF through the movable anchor bases reconfiguration optimization: (a) Movable anchor base ${}^g\mathbf{A}_1$ takes part in the reconfiguration optimization. (b) Movable anchor bases ${}^g\mathbf{A}_1$ and ${}^g\mathbf{A}_2$ take part in the reconfiguration optimization. (c) Movable anchor bases ${}^g\mathbf{A}_1$, ${}^g\mathbf{A}_2$ and ${}^g\mathbf{A}_4$ take part in the reconfiguration optimization. (d) All movable anchor bases take part in the reconfiguration optimization.

## VI. EXPERIMENTS AND RESULTS

### A. *Setup*

Fig. 16 shows the CCRobot-S prototype attached to the bridge cables. Worm gearing was integrated into the transmission chain for the gripper to ensure safety during the experiments. Since the worm gearing is self-locking, the flying platform and the anchor bases could remain in their poses on the stay cables without energy consumption. In addition, brakes were used on the customized winches in case the flying platform fell due to a sudden power outage. Meanwhile, we prepared a multi-cable test platform for the experiments. The performance and capabilities of CCRobot-S were extensively validated and successfully tested on the multi-cable replica, demonstrating its superiority in efficiency, payload, and versatility & agility. The specifications are summarized in Tab. IV.

### B. *Individual Robot Test*

1) Grasping capacity test of the flying platform

In this section, we evaluated the grasping capability of the flying platform. The experimental results shown in Supplementary Video Part II-1 indicate that the flying gripper can adjust its pose to approach and cling to the stay cable through its 3 Degree-of-Freedom (DoF) joints. The flying gripper can lift itself and rotate around its Yaw and Pitch axes. Once the flying gripper attaches itself to the stay cable, the flying platform can maintain its pose and withstand external loads and impacts due to the interlock mechanism without the support of the cable tension. The experimental results demonstrate that the flying platform can maintain its posture under a 15 kg load, which is applied to the side of the flying platform, with the cantilever length measuring approximately 20 cm from the point of application to the center of mass.

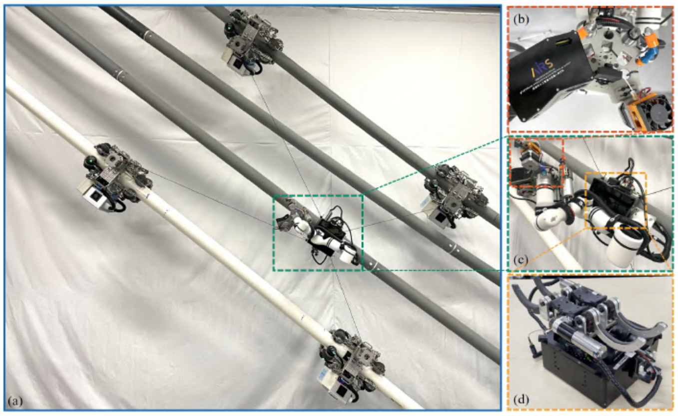

Fig. 16. CCRobot-S prototype and its climbing environment: (a) The prototype of CCRobot-S. (b) The specialized tools unit. (c) The flying platform with a robotic manipulator. (d) The flying platform.

2) Cable-crossing and obstacle-negotiation capacity test of the flying platform

The cable-crossing capability is a distinctive feature of CCRobot-S compared to other cable-climbing robots, contributing to enhanced operational efficiency. In this section, the experimental results demonstrate that the flying platform can detach from one stay cable and then move towards another stay cable without manual removal of the flying platform from one stay cable and installation on another stay cable, as illustrated in Supplementary Video Parts II-2 and -5. Additionally, the obstacle-negotiation capability of the flying platform was also distinct. The flying platform can seamlessly and effortlessly overcome obstacles on the stay cable surfaces. The height of the obstacles that the flying platform can cross depends on the initial distance between the flying platform and the stay cable surface.

3) Climbing motion capacity of the movable anchor base

To assess the motion performance and validate the movable anchor base, we conducted tests both on the indoor testing platform and on a dozen cable-stayed bridges in the field

TABLE IV
SPECIFICATIONS OF CCROBOT-S

| **Parameters** | **Values** |
|---|---|
| Movable anchor base weight | 9 kg |
| Flying platform weight (with RM and ST) | ≈ 30 kg |
| Specialized tools unit weight | 4.5 kg |
| Robotic manipulator weight | 7.8 kg |
| Cable diameter for climbing | 90 – 120 mm |
| Driving cable diameter | 2 mm |
| Dimension of MAB | 48×32×50 cm |
| Dimension of FP (without RM and ST) | 22×22×30 cm |
| MAB static payload with gripper | 25 kg |
| MAB dynamic payload with gripper | 15 kg |
| FP static payload with gripper | 15 kg |
| Maximum climbing angle | 90° |
| Maximum height of obstacle-crossing for MAB | 5 mm |

†MAB = Movable Anchor Base; ‡FP = Flying Platform;
§RM = Robotic Manipulator; ¶ST = Specialized Tools.

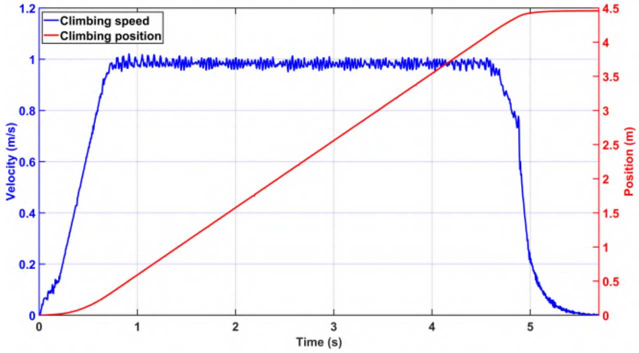

Fig. 17. The variations in climbing speed and position of the movable anchor base during the climbing process.

condition, including Lijiatuo Yangtze River Bridge, Xisha Bridge, Wuling Mountain Bridge, Masangxi Yangtze River Bridge, Dafosi Yangtze River Bridge, and so on by its predecessors. The movable anchor base platform has been tested on more than 500 stay cables, with an accumulated trip of approximately half a million meters. Fig. 17 shows the variations in climbing speed and position of the movable anchor base during a climbing process. The experimental results indicate that the movable anchor base moves smoothly along the stay cable at a maximum climbing speed exceeding 1.0 m/s within a 4.5-meter distance. Additionally, the movable anchor's dynamic and static payloads exceed 15 kg and 25 kg, respectively, demonstrating its capacity to resist cable tension from the flying platform.

### C. *Collaborative Motion Test*

#### 1) Zero-downtime climbing gait

Since the zero-downtime climbing gait is tailored for stay cable inspection, only a high-definition camera is integrated into the flying platform. Given the lightweight feature of the end effector and the simplicity of the operation, the flying platform can move continuously along multiple stay cables and retrieve images without the necessity to halt and adhere to the stay cable. We designed a zigzag trajectory moving and tracking experiment to evaluate the performance of this gait. The experimental task involved crossing over three cables successively and tracking a zigzag trajectory by the flying platform. In this process, we divided the entire trajectory into 150 points, and each moving iteration for the experiment was recorded and shown in Supplementary Video Part II-2. Fig. 18 shows the desired trajectory and the actual trajectory, and the statistical analysis is shown in Fig. 19, the average locomotion errors of the flying platform in the X direction and Y direction are 1.4 ± 9.0 mm and -3.9 ± 10.4 mm, respectively. This indicates that the flying platform's average positioning error is 1.4 mm in the X direction and -3.9 mm in the Y direction, with the flying platform's standard deviations of 9 mm and 10.4 mm, respectively. According to the statistical analysis, we can find that the actual errors can vary around the average caused by the vibration of the flying platform, particularly in the out-of-plane direction for planar configurations. Overall, the system is generally accurate in accomplishing the cable surface inspection task; the experimental results further confirm this cable-crossing capability, enabling the inspection of different stay cable surfaces without re-installing the cable-climbing robot. Consequently, the zero-downtime climbing gait greatly enhances the climbing and operational efficiency within the system.

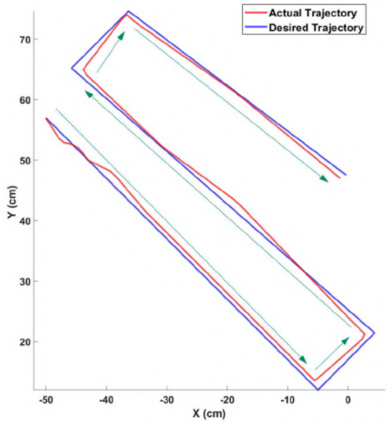

Fig. 18. The comparison between the desired zigzag trajectory and the actual zigzag trajectory climbing along the stay cable.

#### 2) Spider-like climbing gait

Given that the spider-like climbing gait is tailored for stay cable maintenance tasks such as cable grinding, cleaning, or repair, in this section, we integrate a robotic manipulator and a specialized tools unit within the flying platform, totaling approximately 30 kg. Supplementary Video Part II-3 illustrates the climbing sequence of CCRobot-S on a replica of bridge cables. The test results demonstrated that the collaborative robot squad can transport a heavy payload to a designated location and perform maintenance tasks utilizing this climbing gait. Consequently, the spider-like climbing gait enables the system to achieve both a high payload and forceful manipulation capabilities.

#### 3) Inspection and maintenance capacity

In CCRobot-S, several specialized tools are incorporated into the system, including a high-definition camera, pneumatic cleaning head, grinding head, and hot melt gun. Supplementary Video Part II-2 shows the efficient inspection process with a high-definition camera. Since the heavy payload characteristic of this system, it can also carry out maintenance work by transporting the specialized tools to a designated location, as

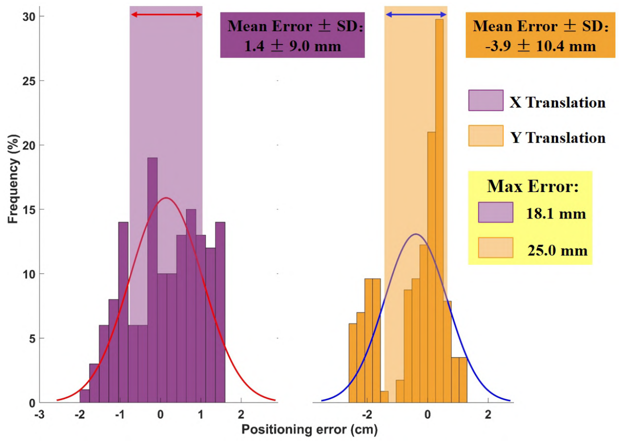

Fig. 19. Statistical graphs of the zigzag trajectory climbing along the stay cable.

**IEEE Transactions on Robotics (T-RO) paper, presented at ICRA 2026, Vienna, Austria. Cite as T-RO paper.**

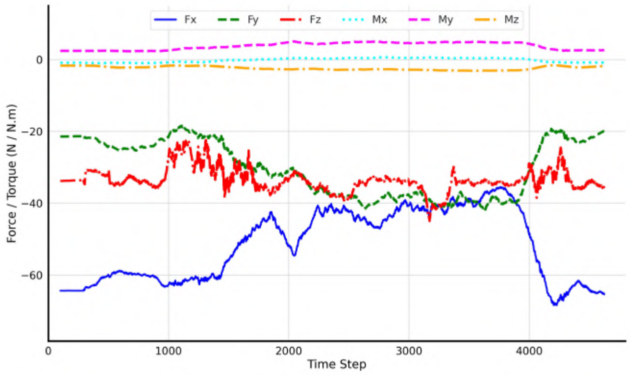

Fig. 20. The variations in force and torque of the robotic manipulator's end-effector during the grinding process.

shown in the Supplementary Video Parts II-3 and -4. Fig. 20 presents the variations in force and torque experienced by the robotic manipulator's end-effector during the grinding process. These variations are captured through feedback from a six-axis force sensor mounted at the end-effector. In the figure, $\mathrm{F}_x$, $\mathrm{F}_y$, and $\mathrm{F}_z$ denote the forces acting on the end-effector along the $x$-, $y$-, and $z$-axes, respectively. Similarly, $\mathrm{M}_x$, $\mathrm{M}_y$, and $\mathrm{M}_z$ represent the torques acting on the end-effector around the $x$-, $y$-, and $z$-axes, respectively. The results show CCRobot-S can accomplish the stay cable surface inspection, cable repairing, and cable grinding, demonstrating the versatility of CCRobot-S.

## VII. CONCLUSIONS AND FUTURE WORKS

This paper introduces a novel methodology and strategy for inspecting and maintaining large-scale, long-span bridge cables through reconfigurable parallel-type cable-driven climbing. The design and implementation of the innovative Collaborative Climbing Robot Squad are detailed, along with the optimization algorithms for grasp arrangement and anchor reconfiguration in the climbing strategy.

- A prototype of CCRobot-S has been developed and validated through various experiments. In summary, CCRobot-S combines high efficiency, heavy-duty capacity, and versatility & agility, advancing state-of-the-art climbing technology. It holds promise for practical applications in the stay cable inspection and maintenance.
- Furthermore, the proposed methodology establishes an innovative climbing paradigm for scenarios with challenging gravity-adversarial large-scale conditions, opening opportunities and paving the way for developing high-quality climbing robotics. Researchers can leverage this approach as a foundation for designing climbing systems in diverse applications.

Moving forward, we plan to integrate an Inertial Measurement Unit (IMU) into the flying platform to enhance pose estimation accuracy compared to the forward kinematics method. We will focus on strengthening the flying platform's disturbance resistance or vibration suppression, particularly in the out-of-plane direction for planar configurations. Additionally, we plan to extend the linear reconfigurable mechanism of the system to a three-dimensional reconfiguration scenario. For instance, integrating a UAV with a flying gripper as a movable anchor base would enable both the flying platform and the movable anchor base to possess the cable-crossing capacity, as shown in Fig. 21. This modification further simplifies the preliminary setup and installation process. It expands the workspace of the robotic system, enabling full automatic inspection or maintenance of all bridge cables without additional manual installation or removal procedures.

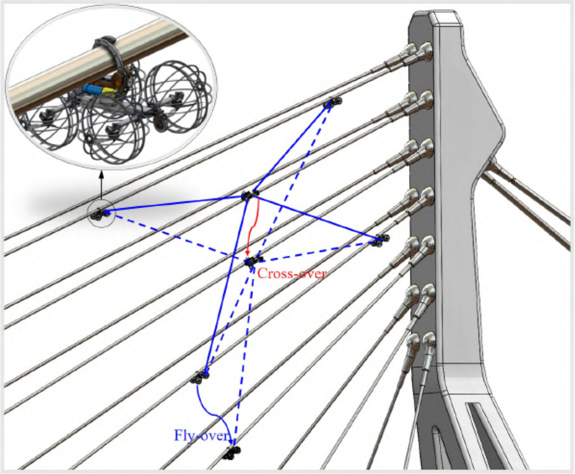

Fig. 21. Concept of more potential CCRobot-S configurations.

## APPENDIX A

### PROOF OF THEOREM 1

*Theorem 1:* For the case of one degree of freedom actuation redundancy cable-driven system or completely constrained cable-driven system where m - n = 1, the state equation is $\mathbf{J}(\mathbf{x}, \mathbf{q}(\mathbf{u}))^{\mathbf{T}}\mathbf{f} + \mathbf{w}_p = 0$, one of the bases of the null space for the transposition of the joint space *Jacobian* $\mathbf{J}(\mathbf{x}, \mathbf{q}(\mathbf{u}))^{\mathbf{T}}$ is derived straightforward from these square matrices obtained from matrix $\mathbf{J}(\mathbf{x}, \mathbf{q}(\mathbf{u}))^{\mathbf{T}}$ by deleting its each column in turn, as shown in Eq. (10) and we abbreviate it as below,

$$Null(\mathbf{J^T}) = \begin{bmatrix} +det\left[\mathbf{J}_2\ \mathbf{J}_3\ \mathbf{J}_4\right] \\ -det\left[\mathbf{J}_1\ \mathbf{J}_3\ \mathbf{J}_4\right] \\ +det\left[\mathbf{J}_1\ \mathbf{J}_2\ \mathbf{J}_4\right] \\ -det\left[\mathbf{J}_1\ \mathbf{J}_2\ \mathbf{J}_3\right] \end{bmatrix}. \tag{29}$$

**Proof:** First, we rewrite the transposition of the joint space *Jacobian* in abbreviation form,

$$\mathbf{J^T} = \begin{bmatrix} j_{11} & j_{12} & j_{13} & j_{14} \\ j_{21} & j_{22} & j_{23} & j_{24} \\ j_{31} & j_{32} & j_{33} & j_{34} \end{bmatrix}, \tag{30}$$

then, we compute the reduced row echelon form (rref) of the matrix $\mathbf{J^T}$,

$$\mathbf{J^T} \xrightarrow{rref} \left[I_{3\times3}\,\middle|\,\mathbf{J}_{3\times3}^{-1}\mathbf{J}_{4\times1}\right], \tag{31}$$

where $\mathbf{J}_{3\times3}^{-1}$ is the inverse matrix of the first $3 \times 3$ first submatrix of $\mathbf{J^T}$, $\mathbf{J}_{4\times1}$ represents the last column of $\mathbf{J^T}$. $I_{3\times3}$ is the identity matrix. Obviously, $\mathbf{v} = [(\mathbf{J}_{3\times3}^{-1}\mathbf{J}_{4\times1})^T \ \ -1]^{\mathbf{T}}$ is one of the bases of the null space vector. Based on that, to prove Theorem 1 is equivalent to proving the following relationship:

$$\begin{bmatrix} +det\left[\mathbf{J}_2\ \mathbf{J}_3\ \mathbf{J}_4\right] \\ -det\left[\mathbf{J}_1\ \mathbf{J}_3\ \mathbf{J}_4\right] \\ +det\left[\mathbf{J}_1\ \mathbf{J}_2\ \mathbf{J}_4\right] \\ -det\left[\mathbf{J}_1\ \mathbf{J}_2\ \mathbf{J}_3\right] \end{bmatrix} \leftrightarrow [(\mathbf{J}_{3\times3}^{-1}\mathbf{J}_{4\times1})^{\mathbf{T}}\ \ -1]^{\mathbf{T}}, \tag{32}$$

meanwhile, the inverse matrix

$$\mathbf{J}_{3\times3}^{-1} = adj(\mathbf{J}_{3\times3})/det(\mathbf{J}_{3\times3}) = (-1)^{i+j}M_{ij}/det(\mathbf{J}_{3\times3}), \tag{33}$$

where $i$ and $j$ are the numbers of rows and columns of the inverse matrix, $M_{ij}$ is the determinant of the $2\times2$ matrix that results from deleting row $i$ and column $j$ of the sub-matrix $\mathbf{J}_{3\times3}$. Because of the homogeneousness property of the basis of the null space vector, we can remove the denominator of the elements in the vector $\mathbf{v}$ by multiplying $det(\mathbf{J}_{3\times3})$, so we can alternatively express the equivalent relationship to be shown as

$$\begin{bmatrix} +det\left[\mathbf{J}_2\ \mathbf{J}_3\ \mathbf{J}_4\right] \\ -det\left[\mathbf{J}_1\ \mathbf{J}_3\ \mathbf{J}_4\right] \\ +det\left[\mathbf{J}_1\ \mathbf{J}_2\ \mathbf{J}_4\right] \\ -det\left[\mathbf{J}_1\ \mathbf{J}_2\ \mathbf{J}_3\right] \end{bmatrix} \leftrightarrow \begin{bmatrix} adj(\mathbf{J}_{3\times3})\mathbf{J}_{4\times1} \\ -det(\mathbf{J}_{3\times3}) \end{bmatrix}. \tag{34}$$

Observing the relationship, we can see that the last elements of the left and right vectors are the same. All we need to do is prove

$$\begin{bmatrix} +det\left[\mathbf{J}_2\ \mathbf{J}_3\ \mathbf{J}_4\right] \\ -det\left[\mathbf{J}_1\ \mathbf{J}_3\ \mathbf{J}_4\right] \\ +det\left[\mathbf{J}_1\ \mathbf{J}_2\ \mathbf{J}_4\right] \end{bmatrix} = \left[adj(\mathbf{J}_{3\times3})\mathbf{J}_{4\times1}\right], \tag{35}$$

meanwhile, $adj(\mathbf{J}_{3\times3})$ can be expressed as:

$$\begin{bmatrix} +\begin{vmatrix} j_{22} & j_{23} \\ j_{32} & j_{33} \end{vmatrix} & -\begin{vmatrix} j_{12} & j_{13} \\ j_{32} & j_{33} \end{vmatrix} & +\begin{vmatrix} j_{12} & j_{13} \\ j_{22} & j_{23} \end{vmatrix} \\ -\begin{vmatrix} j_{21} & j_{23} \\ j_{31} & j_{33} \end{vmatrix} & +\begin{vmatrix} j_{11} & j_{13} \\ j_{31} & j_{33} \end{vmatrix} & -\begin{vmatrix} j_{11} & j_{13} \\ j_{21} & j_{23} \end{vmatrix} \\ +\begin{vmatrix} j_{21} & j_{22} \\ j_{31} & j_{32} \end{vmatrix} & -\begin{vmatrix} j_{11} & j_{12} \\ j_{31} & j_{32} \end{vmatrix} & +\begin{vmatrix} j_{11} & j_{12} \\ j_{21} & j_{22} \end{vmatrix} \end{bmatrix}. \tag{36}$$

To this end, we can calculate that:

$$\begin{cases} \left[adj(\mathbf{J}_{3\times3})\mathbf{J}_{4\times1}\right]_1 = & +\,det\left[\mathbf{J}_2\ \mathbf{J}_3\ \mathbf{J}_4\right] = \\ & j_{22}j_{33}j_{14} - j_{23}j_{32}j_{14} + j_{13}j_{32}j_{24} - \\ & j_{12}j_{33}j_{24} + j_{12}j_{23}j_{34} - j_{22}j_{13}j_{34} \\ \left[adj(\mathbf{J}_{3\times3})\mathbf{J}_{4\times1}\right]_2 = & -\,det\left[\mathbf{J}_1\ \mathbf{J}_3\ \mathbf{J}_4\right] = \\ & j_{21}j_{33}j_{14} - j_{23}j_{31}j_{14} + j_{13}j_{31}j_{24} - \\ & j_{11}j_{33}j_{24} + j_{23}j_{11}j_{34} - j_{13}j_{21}j_{34} \\ \left[adj(\mathbf{J}_{3\times3})\mathbf{J}_{4\times1}\right]_3 = & +\,det\left[\mathbf{J}_1\ \mathbf{J}_2\ \mathbf{J}_4\right] = \\ & j_{22}j_{32}j_{14} - j_{22}j_{31}j_{14} + j_{12}j_{31}j_{24} - \\ & j_{11}j_{32}j_{24} + j_{11}j_{22}j_{34} - j_{21}j_{12}j_{34} \end{cases}. \tag{37}$$

As a result, Eq. (35) is proven, these conditions are equivalent to Eq. (32), indicating that the basis of the null space vector for the state equation $\mathbf{J}(\mathbf{x},\mathbf{q}(\mathbf{u}))^{\mathbf{T}}\mathbf{f} + \mathbf{w}_p = 0$ can be obtained straightforwardly by Eq. (29).

## APPENDIX B

### PROOF OF THEOREM 2

*Theorem 2:* All the components of $Null(\mathbf{J}(\mathbf{x},\mathbf{q}(\mathbf{u}))^{\mathbf{T}})$ in Eq. (29) have the same sign and are not equal to zero *iff* the positive force distribution $\mathbf{f}$ exists, and the pose of the flying platform belongs to the wrench-closure workspace.

**Proof:** As we have deduced in Eq. (31), the state equation can be rewritten as

$$\left[I_{3\times3}\,\middle|\,\mathbf{J}_{3\times3}^{-1}\mathbf{J}_{4\times1}\right]\mathbf{f} = \tilde{\mathbf{w}}_p, \tag{38}$$

where $\tilde{\mathbf{w}}_p$ is the wrench obtained by the reduced row echelon form operation. This equation can be alternatively expressed as

$$f_k + \left[\mathbf{J}_{3\times3}^{-1}\mathbf{J}_{4\times1}\right]_k f_t = [\tilde{\mathbf{w}}_p]_k, \forall k,t \in 1,2,3, \tag{39}$$

where $k,t$ are the $k$th, $t$th row of the matrix $\mathbf{J}^{\mathbf{T}}$, respectively.

Since the tension forces are positive, i.e., $f_k, f_t \in (0,+\infty)$, and the pose of the flying platform is restrained under the wrench-closure condition, i.e.

$$\left\{\mathbf{x} : \forall\tilde{\mathbf{w}}_p, \exists\mathbf{f} > 0, \mathbf{J}^{\mathbf{T}}\mathbf{f} = -\mathbf{w}_p\right\} \leftrightarrow \tilde{\mathbf{w}}_p \in (-\infty,+\infty), \tag{40}$$

Hence, to satisfy the restrained conditions that exist the arbitrary wrench $\tilde{\mathbf{w}}_p$ and positive cable tensions $\mathbf{f}$, each component of the $\left[\mathbf{J}_{3\times3}^{-1}\mathbf{J}_{4\times1}\right]$ should be less than zero, i.e. we have

$$\underbrace{f_k}_{(0+\infty)} + \underbrace{\left[\mathbf{J}_{3\times3}^{-1}\mathbf{J}_{4\times1}\right]_k}_{(-\infty,0)} \underbrace{f_m}_{(0+\infty)} = \underbrace{[\tilde{\mathbf{w}}_p]_k}_{(-\infty,+\infty)}, \forall k \in 1,2,3. \tag{41}$$

Thus, we can conclude that the basis of the null space vector for the state equations $\mathbf{v} \prec 0$, then we translate Eq. (32) into Eq. (34) by removing the denominator of the elements in the vector $\mathbf{v}$ through multiplying $det(\mathbf{J}_{3\times3})$, in such, all the components of $Null(\mathbf{J}^{\mathbf{T}})$ in Eq. (29) have the same sign and not equal to zero, i.e.

$$Null(\mathbf{J}^{\mathbf{T}}) \prec 0 \ \vee \ Null(\mathbf{J}^{\mathbf{T}}) \succ 0. \tag{42}$$

## REFERENCES

[1] sika, "Solutions for bridges and highways." [Online]. Available: https://mys.sika.com/en/solutions-for-projects/bridges.html

[2] K. H. Cho, H. M. Kim, Y. H. Jin, F. Liu, H. Moon, J. C. Koo, and H. R. Choi, "Inspection robot for hanger cable of suspension bridge: Mechanism design and analysis," *IEEE/ASME Transactions on mechatronics*, vol. 18, no. 6, pp. 1665–1674, 2013.

[3] K. H. Cho, Y. H. Jin, H. M. Kim, and H. R. Choi, "Development of novel multifunctional robotic crawler for inspection of hanger cables in suspension bridges," in *2014 IEEE international conference on robotics and automation (ICRA)*. IEEE, 2014, pp. 2673–2678.

[4] K. H. Cho, Y. H. Jin, H. M. Kim, H. Moon, J. C. Koo, and H. R. Choi, "Multifunctional robotic crawler for inspection of suspension bridge hanger cables: Mechanism design and performance validation," *IEEE/ASME Transactions on Mechatronics*, vol. 22, no. 1, pp. 236–246, 2016.

[5] IPC, "Cablescan® cable stayed bridge inspection service," 2015. [Online]. Available: https://www.infrastructurepc.com/cablescan/

[6] F. Xu, X. Wang, and L. Wang, "Cable inspection robot for cable-stayed bridges: Design, analysis, and application," *Journal of Field Robotics*, vol. 28, no. 3, pp. 441–459, 2011.

[7] S. T. Nguyen, K. T. La, and H. M. La, "Agile robotic inspection of steel structures: A bicycle-like approach with multisensor integration," *Journal of Field Robotics*, vol. 41, no. 2, pp. 396–419, 2024.

[8] M. Tavakoli, G. Cabrita, R. Faria, L. Marques, and A. T. de Almeida, “Cooperative multi-agent mapping of three-dimensional structures for pipeline inspection applications,” *The International Journal of Robotics Research*, vol. 31, no. 12, pp. 1489–1503, 2012.

[9] F. Xu, S. Dai, Q. Jiang, and X. Wang, “Developing a climbing robot for repairing cables of cable-stayed bridges,” *Automation in Construction*, vol. 129, p. 103807, 2021.

[10] J. Luo, S. Xie, Z. Gong, and T. Lu, “Development of cable maintenance robot for cable-stayed bridges,” *Industrial Robot: An International Journal*, vol. 34, no. 4, pp. 303–309, 2007.

[11] J. Li, X. Liu, S. Jiang, R. Li, and L. Ren, “Design of continuous climbing pneumatic cable maintenance robot,” in *Mechatronics and Automation, 2009. ICMA 2009. International Conference on*. IEEE, 2009, pp. 4633–4637.

[12] J. Yuan, X. Wu, Y. Kang, and A. Ben, “Research on reconfigurable robot technology for cable maintenance of cable-stayed bridges in-service,” in *2010 International Conference on Mechanic Automation and Control Engineering*. IEEE, 2010, pp. 1019–1022.

[13] Z. Zheng, X. Yuan, X. Yu, and N. Ding, “Mechanical design of a climbing robot for inspection on a cable-stayed bridge,” in *The World Congress on Intelligent Control and Automation (WCICA)*, Changsha, Hunan, China, 2018, pp. 1680–1684.

[14] Z. Zheng, S. Hu, and N. Ding, “A biologically inspired cable climbing robot: Ccrobot-design and implementation,” in *2018 IEEE International Conference on Robotics and Biomimetics (ROBIO)*. IEEE, 2018, pp. 2354–2359.

[15] Z. Zheng and N. Ding, “Design and implementation of ccrobot-ii: a palm-based cable climbing robot for cable-stayed bridge inspection,” in *2019 International Conference on Robotics and Automation (ICRA)*. IEEE, 2019, pp. 9747–9753.

[16] N. Ding, Z. Zheng, J. Song, Z. Sun, T. L. Lam, and H. Qian, “Ccrobot-iii: a split-type wire-driven cable climbing robot for cable-stayed bridge inspection,” in *2020 IEEE International Conference on Robotics and Automation (ICRA)*. IEEE, 2020, pp. 9308–9314.

[17] W. Zhang, Z. Zheng, X. Fu, S. Hazken, H. Chen, M. Zhao, and N. Ding, “Ccrobot-iv-f: a ducted-fan-driven flying-type bridge-stay-cable climbing robot,” in *2021 IEEE/RSJ International Conference on Intelligent Robots and Systems (IROS)*. IEEE, 2021, pp. 4184–4190.

[18] Z. Zheng, W. Zhang, X. Fu, S. Hazken, X. Hu, H. Chen, J. Luo, and N. Ding, “Ccrobot-iv: An obstacle-free split-type quad-ducted propeller-driven bridge stay cable-climbing robot,” *IEEE Robotics and Automation Letters*, vol. 7, no. 4, pp. 11 751–11 758, 2021.

[19] Z. Zheng, N. Ding, H. Chen, X. Hu, Z. Zhu, X. Fu, W. Zhang, L. Zhang, S. Hazken, Z. Wang *et al.*, “Ccrobot-v: A silkworm-like cooperative cable-climbing robotic system for cable inspection and maintenance,” in *2022 International Conference on Robotics and Automation (ICRA)*. IEEE, 2022, pp. 164–170.

[20] Z. Zheng, C. Wang, X. Hu, L. Zhang, W. Zhang, Y. Xu, P. Liu, X. Pang, T. L. Lam, and N. Ding, “Developing a climbing robot for stay cable maintenance with security and rescue mechanisms,” *Journal of Field Robotics*, 2025.

[21] F. Xu, X. Wang, and P. Cao, “Design and application of a new wheel-based cable inspection robot,” in *2011 IEEE International Conference on Robotics and Automation (ICRA)*. IEEE, 2011, pp. 4909–4914.

[22] F. Xu, J. L. Hu, X. Wang, and G. Jiang, “Helix cable-detecting robot for cable-stayed bridge: Design and analysis,” *International Journal of Robotics and Automation*, vol. 29, no. 4, pp. 406–414, 2014.

[23] F. Xu, J. Hu, and G. Jiang, “The obstacle-negotiation capability of rod-climbing robots and the improved mechanism design,” *Journal of Mechanical Science and Technology*, vol. 29, no. 7, pp. 2975–2986, 2015.

[24] T. L. Lam and Y. Xu, “Climbing strategy for a flexible tree climbing robot treebot,” *IEEE transactions on robotics*, vol. 27, no. 6, pp. 1107–1117, 2011.

[25] H. M. La, T. H. Dinh, N. H. Pham, Q. P. Ha, and A. Q. Pham, “Automated robotic monitoring and inspection of steel structures and bridges,” *Robotica*, vol. 37, no. 5, pp. 947–967, 2019.

[26] S. T. Nguyen and H. M. La, “A climbing robot for steel bridge inspection,” *Journal of Intelligent & Robotic Systems*, vol. 102, no. 4, p. 75, 2021.

[27] S. T. Nguyen, A. Q. Pham, C. Motley, and H. M. La, “A practical climbing robot for steel bridge inspection,” in *2020 IEEE International Conference on Robotics and Automation (ICRA)*. IEEE, 2020, pp. 9322–9328.

[28] H.-D. Bui, S. Nguyen, U. H. Billah, C. Le, A. Tavakkoli, and H. M. La, “Control framework for a hybrid-steel bridge inspection robot,” in *2020 IEEE/RSJ International Conference on Intelligent Robots and Systems (IROS)*. IEEE, 2020, pp. 2585–2591.

[29] H. Ahmed, S. T. Nguyen, D. La, C. P. Le, and H. M. La, “Multi-directional bicycle robot for bridge inspection with steel defect detection system,” in *2022 IEEE/RSJ International Conference on Intelligent Robots and Systems (IROS)*. IEEE, 2022, pp. 4617–4624.

[30] Y. Otsuki, S. T. Nguyen, H. M. La, and Y. Wang, “Autonomous ultrasonic thickness measurement of steel bridge members using a climbing bicycle robot,” *Journal of Engineering Mechanics*, vol. 149, no. 8, p. 04023051, 2023.

[31] Wikipedia, “Russky bridge.” [Online]. Available: https://en.wikipedia.org/wiki/RusskyBridge

[32] C. Edmonds, K. O’Neill, X. Koscher, B. Murphy, and R. Oates, “Anzac bridge maintenance project,” in *Austroads Bridge Conference, 8th, 2011, Sydney, New South Wales, Australia*, no. AP-G90/11, 2011.

[33] BostonDynamics, “Spot the agile mobile robot.” [Online]. Available: https://bostondynamics.com/products/spot/

[34] M. Hutter, C. Gehring, M. A. Höpflinger, M. Blösch, and R. Siegwart, “Toward combining speed, efficiency, versatility, and robustness in an autonomous quadruped,” *IEEE Transactions on Robotics*, vol. 30, no. 6, pp. 1427–1440, 2014.

[35] P. M. Wensing, A. Wang, S. Seok, D. Otten, J. Lang, and S. Kim, “Proprioceptive actuator design in the mit cheetah: Impact mitigation and high-bandwidth physical interaction for dynamic legged robots,” *IEEE transactions on robotics*, vol. 33, no. 3, pp. 509–522, 2017.

[36] M. Spenko, G. C. Haynes, J. Saunders, M. R. Cutkosky, A. A. Rizzi, R. J. Full, and D. E. Koditschek, “Biologically inspired climbing with a hexapedal robot,” *Journal of Field Robotics*, vol. 25, no. 4-5, pp. 223–242, 2008.

[37] M. A. Estrada, S. Mintchev, D. L. Christensen, M. R. Cutkosky, and D. Floreano, “Forceful manipulation with micro air vehicles,” *Science Robotics*, vol. 3, no. 23, p. eaau6903, 2018.

[38] A. Parness, M. Frost, N. Thatte, J. P. King, K. Witkoe, M. Nevarez, M. Garrett, H. Aghazarian, and B. Kennedy, “Gravity-independent rock-climbing robot and a sample acquisition tool with microspine grippers,” *Journal of Field Robotics*, vol. 30, no. 6, pp. 897–915, 2013.

[39] S. Hong, Y. Um, J. Park, and H.-W. Park, “Agile and versatile climbing on ferromagnetic surfaces with a quadrupedal robot,” *Science Robotics*, vol. 7, no. 73, p. eadd1017, 2022.

[40] S. B. Backus, R. Onishi, A. Bocklund, A. Berg, E. D. Contreras, and A. Parness, “Design and testing of the jpl-nautilus gripper for deep-ocean geological sampling,” *Journal of Field Robotics*, vol. 37, no. 6, pp. 972–986, 2020.

[41] B. Katz, J. Di Carlo, and S. Kim, “Mini cheetah: A platform for pushing the limits of dynamic quadruped control,” in *2019 international conference on robotics and automation (ICRA)*. IEEE, 2019, pp. 6295–6301.

[42] D. L. Christensen, E. W. Hawkes, S. A. Suresh, K. Ladenheim, and M. R. Cutkosky, “$\mu$tugs: Enabling microrobots to deliver macro forces with controllable adhesives,” in *2015 IEEE International Conference on Robotics and Automation (ICRA)*. IEEE, 2015, pp. 4048–4055.

[43] M. Kovac, “Learning from nature how to land aerial robots,” *Science*, vol. 352, no. 6288, pp. 895–896, 2016.

[44] T. Miki, P. Khrapchenkov, and K. Hori, “Uav/ugv autonomous cooperation: Uav assists ugv to climb a cliff by attaching a tether,” in *2019 International Conference on Robotics and Automation (ICRA)*. IEEE, 2019, pp. 8041–8047.

[45] J. Quan and D. Hong, “Flexible long-reach robotic limbs using tape springs for mobility and manipulation,” *Journal of Mechanisms and Robotics*, vol. 15, no. 3, p. 031009, 2023.

[46] R. R. SUDIONO, Y. SUGAHARA, M. ENDO, D. MATSUURA, and Y. TAKEDA, “Cable traversing robots on spatially structured cableway for reconfigurable parallel cable system,” in *The Proceedings of JSME annual Conference on Robotics and Mechatronics (Robomec) 2019*. The Japan Society of Mechanical Engineers, 2019, pp. 1A1–S02.

[47] T. L. Lam and Y. S. Xu, *Tree climbing robot: design, kinematics and motion planning*. Springer, 2012, vol. 78.

[48] T. L. Lam and Y. Xu, “Biologically inspired tree-climbing robot with continuum maneuvering mechanism,” *Journal of Field Robotics*, vol. 29, no. 6, pp. 843–860, 2012.

[49] ——, “Motion planning for tree climbing with inchworm-like robots,” *Journal of Field Robotics*, vol. 30, no. 1, pp. 87–101, 2013.

[50] G. Abbasnejad, J. Eden, and D. Lau, “Generalized ray-based lattice generation and graph representation of wrench-closure workspace for arbitrary cable-driven robots,” *IEEE Transactions on Robotics*, vol. 35, no. 1, pp. 147–161, 2018.